

Broadband Radiative Quantities for the EarthCARE Mission: The ACM-COM and ACM-RT Products

Jason N. S. Cole¹, Howard W. Barker², Zhipeng Qu¹, Najda Villefranque³, Mark W. Shepherd¹

¹ Environment and Climate Change Canada, Toronto, ON, Canada

² Environment and Climate Change Canada, Victoria, ON, Canada

³ Centre National de Recherches Météorologiques, Météo France / CNRS, Toulouse, France

Correspondence to: Howard W. Barker (howard.barker@canada.ca)

Abstract. The EarthCARE satellite mission’s objective is to retrieve profiles of aerosol and water cloud physical properties from measurements made by its cloud-profiling radar, backscattering lidar, and passive multi-spectral spectral imager (MSI). These retrievals, together with other geophysical properties, are input into broadband (BB) radiative transfer (RT) models that predict radiances, and fluxes, commensurate with measurements made, and inferred from, EarthCARE’s BB radiometer (BBR). The scientific goal is that modelled and “observed” BB fluxes differ, on average, by less than $\pm 10 \text{ W m}^{-2}$. When sound synergistic retrievals from the ACM-CAP process are available, they are acted on by the RT models. When they are not available, the RT models act on “composite” profiles of properties retrieved from measurements made by individual sensors. “Compositing” is performed in the ACM-COM process..

The majority of this report describes the RT models, and their products, that make-up EarthCARE’s ACM-RT process. Profiles of BB shortwave (SW) and longwave (LW) fluxes and heating rates (HR) are computed by 1D RT models for each $\sim 1 \text{ km}$ nadir column of inferred properties. 3D RT models compute radiances for the BBR’s three viewing directions, with the SW model also computing flux and HR profiles; the 3D LW model produces upwelling flux at just one level. All 3D RT products are averages over $5 \times 21 \text{ km}$ “assessment domains” that are constructed using MSI data. Some of ACM-RT’s products are passed forward to the “radiative closure assessment” process that quantifies, for each assessment domain, the likelihood that EarthCARE’s goal has been achieved. As EarthCARE represents the first mission to make “operational” use of 3D RT models, emphasis is placed on differences between 1D and 3D RT results. For upwelling SW flux at 20 km altitude, 1D and 3D values can be expected to differ by more than EarthCARE’s scientific goal of $\pm 10 \text{ W m}^{-2}$ at least 50% of the time.

1. Introduction

The EarthCARE satellite mission's primary objective is to make avant-garde observations of Earth's atmosphere that
 30 can be used to help improve representations of clouds and aerosols in numerical models that predict weather, air
 quality, and climatic change (Illingworth et al. 2015). Detailed descriptions of observations made by EarthCARE's
 cloud-profiling radar (CPR), backscattering lidar (ATLID), passive multi-spectral imager (MSI), and broadband
 radiometer (BBR), as well as the L2-retrieval algorithms that operate on them, are discussed in several papers of this
 35 special issue (Eisinger et al. 2023). EarthCARE's scientific goal is to retrieve cloud and aerosol properties with
 enough accuracy that when operated on by broadband (BB) radiative transfer (RT) models, their estimated top-of-
 atmosphere (TOA) BB fluxes, for domains covering $\sim 100 \text{ km}^2$, agree, more often than not, with their BBR-derived
 40 counterparts (Velázquez-Blázquez et al. 2023a) to within $\pm 10 \text{ W m}^{-2}$ (ESA 2001). This "radiative closure assessment", which marks the end of the initial version of EarthCARE's formal "data production chain", provides a continuous
 radiative closure assessment of L2 retrievals with invaluable information to both L2-algorithm developers and
 45 data users.

The primary purpose of this paper is to describe and demonstrate the BB RT models used for both radiative closure
 assessment and provision of BB flux and heating rate (HR) profiles. Application of BB RT models to L2-retrieval
 products, along with auxiliary data, such as profiles of state variables and surface optical properties, will provide
 estimates of a range of diagnostic radiative flux and HR profiles. Examples of these products are presented here for
 45 simulated conditions along $\sim 6,200 \text{ km}$ -long sections of EarthCARE orbits, which are referred to as "frames" (Qu et
 al. 2023). These simulations underpin most experiments reported in this special issue.

Both 1D and 3D shortwave (SW) and longwave (LW) RT models are used. Both SW and LW 3D models produce
 TOA radiances; the SW model also produces flux and HR profiles for all-sky conditions for a subset of $\sim 100 \text{ km}^2$
 assessment domains, while the LW model produces upwelling fluxes at a single level. The number of radiative
 50 closure assessment domains that can be processed per frame changes from frame-to-frame and will depend on com-
 puter resource availability during the mission as well as, to a lesser extent, cloud structure. Both SW and LW 1D
 models produce flux and HR profiles for each L2-column for all-sky, clear-sky (i.e., clouds removed), and pristine-
 sky (i.e., cloud and aerosol removed) conditions. This provides continuity with previous and ongoing missions such
 as CloudSat (Stephens et al. 2002) and CERES (Wielicki et al. 1996). All applications of RT models occur in the

55 processor referred to as ACM-RT. As for other EarthCARE’s processors, the prefix indicates instrument(s) whose data provide input data, while the suffix represents an abbreviation of the current processor; in this case, ACM stands for ATLID;CPR;MSI and RT for Radative Transfer.

The current plan is for RT models to be applied to cloud and aerosol profile retrievals from the ACM-CAP (CAP: Clouds, Aerosols and Precipitation) process’s Cloud, Aerosol and Precipitation from mulTiple Instruments using a 60 VAriational TEchnique (CAPTIVATE) algorithm (Mason et al. 2023). ACM-CAP’s products, which are in the L2b class of products, are recognized formally as EarthCARE’s “best estimates” for they represent the most complete, synergistic, use of observations made by the CPR, ATLID, and MSI. Should CAPTIVATE fail, the contingency plan is to use a *composite* back-up “best estimate” based on products arising from retrieval algorithms that operate on measurements from a single active sensor. These products are in the L2a class. As such, the secondary purpose of 65 this paper is to describe how the composite cloud and aerosol profiles are generated within the ACM-COM (COM: COMposite) process.

The following section provides an overview of the ACM-COM and ACM-RT processes and how they link to other processes. This is followed by a description of how EarthCARE retrievals are prepared for use in RT models including the creation of L2a-composite (back-up) cloud-aerosol profiles. In section 4 the SW and LW RT models are 70 described along with atmospheric and surface optical properties. RT model results are documented in section 5 making use of the synthetic test frames. This includes showing the full extent of products from the 1D models and differences between SW and LW fluxes predicted by 1D and 3D RT models. Section 6 provides a summary.

2. Overview of EarthCARE’s radiation products

Figure 1 encapsulates the main operations of ACM-COM and ACM-RT including its inputs and outputs. ACM-75 COM prepares profiles of cloud and aerosol properties, produced by L2-retrieval processors as summarized by Eisinger et al. (2023), for use by the BB RT models in ACM-RT. Main operations of these processors are addressed in the subsequent two sections. The remainder of this section provides an overview of the components in Figure 1.

Arriving at ACM-COM are profiles of cloud and aerosol properties for each column, in the mission’s joint standard grid (JSG) (Eisinger et al. 2023), along the L2-plane as retrieved by single active sensor L2a algorithms. ACM-COM 80 also receives similar profiles produced by the synergistic L2b CAPTIVATE algorithm in ACM-CAP, which utilizes

ATLID, CPR, and MSI measurements (Mason et al. 2023). While studies to date suggest that ACM-CAP products will likely be EarthCARE’s default “best estimates” (Mason et al. 2023a), this will not be known for sure until EarthCARE’s post-launch “commissioning phase”. Should ACM-CAP fail, and thus leave only (some) L2a retrievals remain usable by RT models, a contingency plan was developed in which L2a products are merged to form alternate

85 “best estimate” composite cloud-aerosol profiles. Compositing of L2a products is explained in section 3.2.

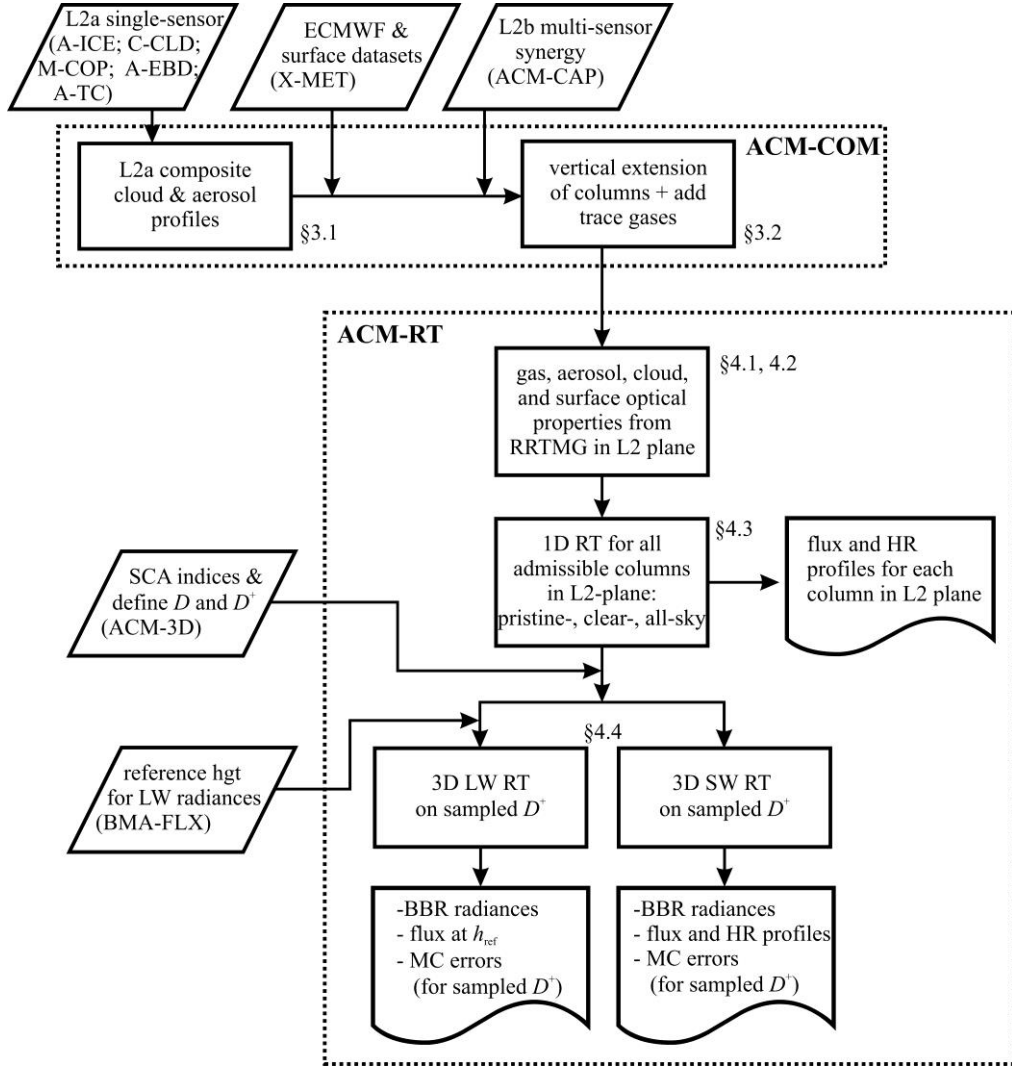


Figure 1. Flowchart summarizing the basic inputs to the ACM-COM and ACM-RT processes, their core operations, and their permanent output files. The operations are discussed in sections listed next to them.

90 Regardless of whether ACM-CAP or alternate L2a-composite profiles are acted on by ACM-RT’s RT models, they need to be readied for use there. Hence, the last steps of ACM-COM take profiles of meteorological variables and

surface conditions, passed in from the auXiliary METeorology (X-MET) processor (Eisinger et al. 2023) and databases, respectively, and merge them with ACM-CAP or L2a-composite products.

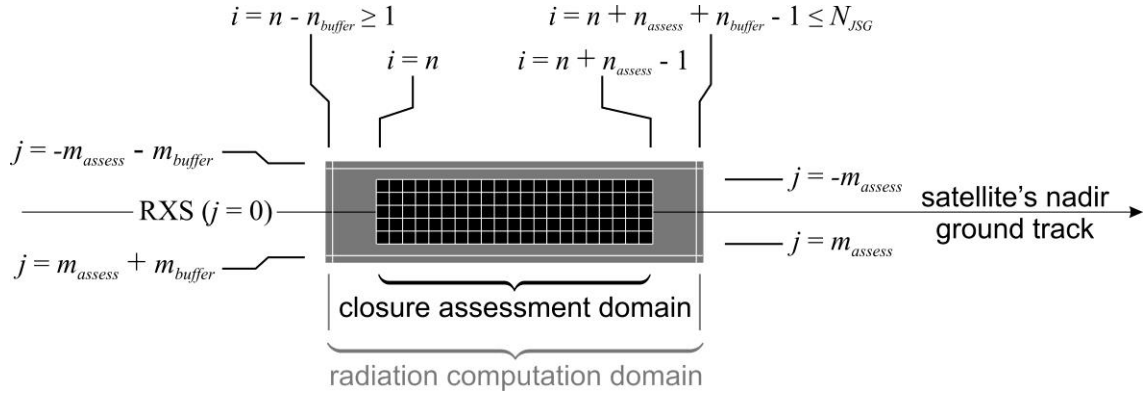
Following previous satellite missions (e.g., L'Ecuyer et al. 2008; Kato et al. 2013), ACM-RT computes SW and LW

95 BB flux and HR profiles by applying 1D RT models to each admissible JSG profile along the L2-plane. EarthCARE makes a substantial step forward, however, with its operational use of 3D BB RT models for both SW and LW bands. For consistency, 1D and 3D models use, where possible, common descriptions of atmospheric and surface optical properties. Optical properties for pristine atmospheres, free of aerosol and cloud, come from the Rapid Radiative Transfer Model for General Circulation Models (RRTMG) (Iacono et al. 2008; Morcrette et al. 2008). RRTMG's 100 SW and LW 1D two-stream models compute flux and HR profiles for each JSG column along the L2-plane. The default is to use all ACM-CAP profiles available in an EarthCARE frame. If no ACM-CAP profiles are available, or if there is an explicit request for radiative closure assessment to be performed on ACM-COM results, radiative transfer calculations are performed for the L2a-composite profiles. These results are passed to ACMB-DF (B:BBR, DF: Difference of Fluxes) (Barker et al. 2023) where they are averaged over "radiative closure assessment domains" 105 D as dictated by the ACMB-3D (3D: 3 Dimensional) scene construction algorithm indices (Qu et al. 2023).

The 3D RT solvers are Monte Carlo solutions of the plane-parallel 3D RT equation. They use the same gaseous, aerosol, and cloud optical properties as the 1D models, but they use detailed scattering phase functions. The SW model produces profiles of fluxes and HRs, and TOA BB radiances commensurate with the BBR's three telescopes.

The LW model computes the same radiances along with an upwelling flux at a "reference height" as defined in the

110 (BMA-FLX) (FLX: FLuXes) process (Velázquez-Blázquez et al. 2023a). All 3D RT computations are done for "radiation computation domains" D^+ that consist of D and buffer-zones around them (see *Figure 2*). Model-estimates of radiances and fluxes, and any available uncertainties, are averaged over D and passed to the ACMB-DF processor (Barker et al. 2023) where they are compared to BBR radiances and their model-derived fluxes (Velázquez-Blázquez et al. 2023a, Velázquez-Blázquez et al. 2023b).



115

Figure 2: Schematic showing the radiative closure assessment domain D (black) and extended computation domain D^+ (shaded), which is the union of D and its buffer-zones. These domains are centred on the L2a/L2b retrieved cross-section (RXS). See Qu et al. (2023) for details.

120

3. ACM-COM: Preparations for RT models and L2a-composites

As described in the next subsection, ACM-COM readies, for use by RT models in ACM-RT, cloud and aerosol information from various L2-retrieval processes and meteorological information from X-MET. This is followed by an explanation of how ACM-CAP's alternate *L2-composite profiles* are produced.

3.1. Prepping L2-retrievals for RT models

125 The ACM-COM process begins by simply extracting, from X-MET files, information about atmospheric state as needed by all BB RT models. This includes profiles of pressure, temperature, humidity, and ozone concentration. Regarding aerosols, their classification information is provided by the AC-TC (TC: Target Classification) processor (Irbah et al. 2023) with extinction profiles at $0.355 \mu\text{m}$ obtained from the A-EBD (EBD: Extinction Backscatter Depolarization) product (Donovan et al. 2023). Six types of aerosols are considered: dust, sea salt, continental pollution, smoke, dusty smoke, and dusty mix. Grid-cells in AC-TC that are classed as *cloudy*, *uncertain*, *missing*, or *noisy* are considered to be aerosol-free.

130 Additionally, ACM-COM adds the following minor molecular species to X-MET profiles: CO_2 , CH_4 , N_2O , CFC-11, CFC-12, CFC-22, and CCL4. These profiles come from climatologies generated by J.-J. Morcrette and A. Bozzo (per. comm., R. Hogan 2013). Values are functions of month, pressure, and latitude.

135 **3.2. Construction of “L2a-composite” cloud and aerosol profiles**

This subsection describes the algorithm that produces the alternate to ACM-CAP’s synergistic L2b “best estimates”, It is based on compositing L2a cloud microphysical property retrievals from A-ICE (ICE: ICE microphysical estimation) (Donovan et al. 2023) and C-CLD (CLD: CLouD) (Mroz et al. 2023) products.

The L2a-composite’s cloud properties depend on an indication of columnar cloudiness from the M-COP (COP: 140 Cloud Optical Properties) processor (Hünerbein et al. 2023). If a grid-cell in a column has *either* A-ICE or C-CLD cloud water content greater than zero, the reported cloud properties enter directly into the L2a-composite. If, however, *both* A-ICE and C-CLD report valid cloud properties with ice water contents $IWC > 0$, aggregated normalized uncertainties for IWC and crystal effective radius r_{eff} are computed, respectively, as

$$\sigma_{A-ICE} = \sqrt{\left(\frac{\sigma_{IWC}^{A-ICE}}{IWC^{A-ICE}}\right)^2 + \left(\frac{\sigma_{r_{eff}}^{A-ICE}}{r_{eff}^{A-ICE}}\right)^2} \quad \text{and} \quad \sigma_{C-CLD} = \sqrt{\left(\frac{\sigma_{IWC}^{C-CLD}}{IWC^{C-CLD}}\right)^2 + \left(\frac{\sigma_{r_{eff}}^{C-CLD}}{r_{eff}^{C-CLD}}\right)^2}, \quad (1)$$

145 where σ_{IWC}^{A-ICE} , σ_{IWC}^{C-CLD} , $\sigma_{r_{eff}}^{A-ICE}$, and $\sigma_{r_{eff}}^{C-CLD}$ are processor-specific 1-sigma uncertainties. Ice cloud properties for the product having $\min(\sigma_{A-ICE}, \sigma_{C-CLD})$ enter into the L2a-composite. For grid-cells designated to contain only liquid cloud, C-CLD properties are used. Hence, L2a-composites resemble NASA’s CloudSat-CALIPSO-CERES (C3M) product (Kato et al. 2010), though it is simpler in that active sensor-derived water contents are *not* constrained, as they are in ACM-CAP, by MSI passive radiances.

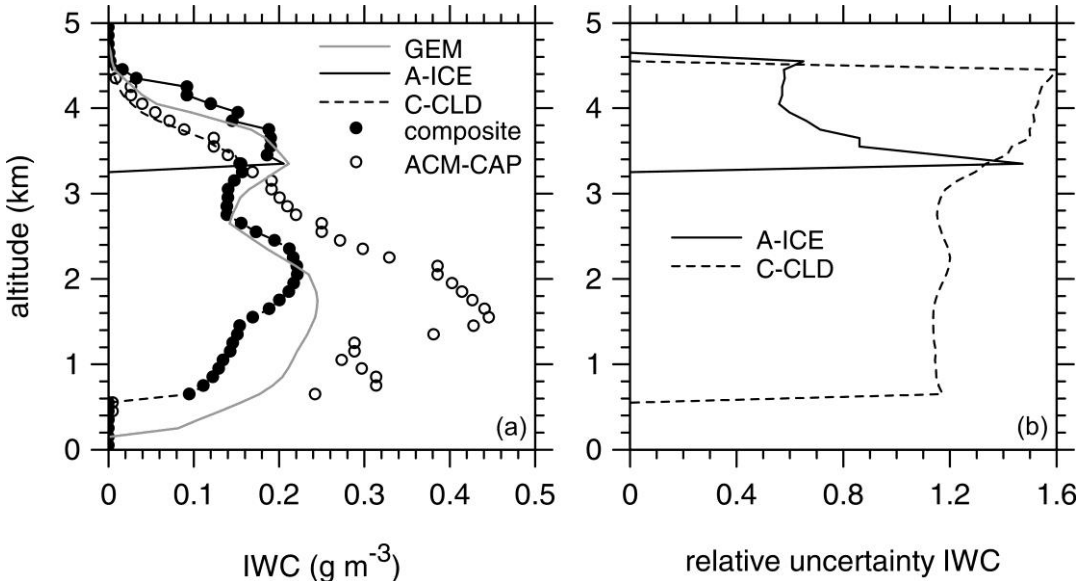


Figure 3: (a) Lines represent profiles of IWC directly from the test frame (simulated by GEM), as well as those retrieved by the L2a algorithms in processors A-ICE and C-CLD. Filled circles are layer values that ACM-COM's algorithm selected from A-ICE and C-CLD according to which one has the smallest aggregated relative uncertainty, defined by (1), as shown in (b). This profile, which has only ice cloud, is from the *Halifax* test frame at 63.67°N, 54.64°W.

Figure 3 shows an example of this compositing process for a column from a simulated frame (Qu et al. 2023). Only ice cloud was present, so both A-ICE and C-CLD reported hydrometeors. Above ~3.4 km ATLID's estimates have least uncertainty meaning that A-ICE values enter into the composite. At ~3.3 km the CPR value is least uncertain and so C-CLD's estimate is used. As ATLID failed to return useable signals at lower altitudes, CPR values fill the remainder of ACM-COM's profile.

In this example, the “reference values”, as simulated by the Global Environmental Multi-scale (GEM) model (Qu et al. 2023), generally match ACM-COM's better than ACM-CAP's. This, however, does not mean that ACM-COM profiles will be used by the RT models. First, during the mission “reference values” are, of course, unknown so a plot like Figure 3 cannot be made or used. Second, if and when ACM-CAP profiles exist, they are used by default.

4. ACM-RT: Broadband radiative transfer models

As mentioned above, EarthCARE's RT models are based on RRTMG (Iacono et al. 2003, 2008; Morcrette et al. 2008). Like its computationally taxing progenitor (Mlawer et al. 1997; Mlawer and Clough 1998), RRTMG is built

on the correlated k -distribution (CKD) method (Goody et al. 1989; Lacis and Oinas 1991). Broadband integrated flux
170 and HR profiles are sums of calculations for quadrature points (112 for SW and 140 for LW) spread over spectral bands (14 for SW and 16 for LW, *Table 1*). RRTMG is used widely in large-scale models, and its verification has been documented elsewhere (e.g., Iacono et al. 2008; Oreopoulos et al. 2012). This section begins by describing atmospheric and surface optical properties, and follows with descriptions of the 1D and 3D transport solvers.

4.1. Optical properties: Atmospheric constituents

175 4.1.1. Gases

Molecular optical depths are computed by the CKD method in RRTMG_SW_v3.9 and RRTMG_LW v4.85 for several wavenumber intervals (*Table 1*) and used by both 1D and 3D RT models. The SW CKD model accounts for absorption by H_2O , CO_2 , O_3 , CH_4 , O_2 , and N_2 plus Rayleigh scattering while the LW CKD model accounts for absorption by H_2O , CO_2 , O_3 , N_2O , CH_4 , O_2 , N_2 , CFC11, CFC12, CFC22, and CCl_4 . A continuum model, CKD_v2.4,
180 accounts for foreign- and self-broadening of lines for H_2O , CO_2 , O_2 , O_3 , and Rayleigh scattering. Molecular absorption coefficients for RRTMG's k -distributions were obtained from the *line-by-line* RT model (LBLRTM), which has been evaluated against surface and laboratory observations (Clough et al. 2005; Shephard et al. 2009; Alvarado et al.
185 2012). LBLRTM's spectroscopic line parameters are essentially equivalent to HITRAN 2000 and HITRAN 1996 (SW) databases. Algorithmic accuracy of LBLRTM is 0.5% (Clough et al. 2005) with limiting errors generally attributed to line shape and spectroscopic input parameters.

Table 1. Wavenumber intervals used in SW and LW RRTMG models. Wavenumbers are in cm^{-1} .

SW	2600	3250	4000	4650	5150	6150	7700	8050	12850	16000	22650	29000	38000	820
	3250	4000	4650	5150	6150	7700	8050	12850	16000	22650	29000	38000	50000	2600
LW	10	350	500	630	700	820	980	1080	1180	1390	1480	1800	2080	2250
	350	500	630	700	820	980	1080	1180	1390	1480	1800	2080	2250	2380
														2600
														3250

For 1D SW RT, the Rayleigh scattering phase function is approximated as $p_{\text{Ray}}(\mu) = 1$, where $\mu = \cos \theta$ and θ is scattering angle. For 3D SW RT, on the other hand,

190
$$p_{Ray}(\mu) = \frac{3}{4}(1 + \mu^2), \quad (2)$$

which is, as are all phase functions used here, normalized as

$$\frac{1}{2} \int_{-1}^1 p_{Ray}(\mu) d\mu = 1. \quad (3)$$

Relative to LBLRTM, clear-sky RRTMG_LW BB fluxes at all levels are accurate to within $\pm 1.5 \text{ W m}^{-2}$ ($\pm 1 \text{ W m}^{-2}$ for direct-beam and $\pm 2 \text{ W m}^{-2}$ for diffuse-beam), with HRs agreeing to within $\pm 0.2 \text{ K day}^{-1}$ in the troposphere and
195 $\pm 0.4 \text{ K day}^{-1}$ in the stratosphere. Likewise, RRTMG_SW's accuracies, at $\mu_0 \approx 0.7$, are within $\pm 3 \text{ W m}^{-2}$ at all levels, with HRs agreeing to within $\pm 0.1 \text{ K day}^{-1}$ in the troposphere, and $\pm 0.35 \text{ K day}^{-1}$ in the stratosphere.

4.1.2. Aerosols

As with gases, 1D and 3D RT models share the same spectral optical properties for aerosols: extinction coefficient β_{aero} , single-scattering albedo ω_{aero} , and asymmetry parameter g_{aero} . Spectral β_{aero} , ω_{aero} , and g_{aero} are averaged over wavelength λ intervals listed above, and were generated so as to be consistent with retrieval algorithms
200 following Wandinger et al. (2023). Radiative properties for their basic aerosol types are then mixed externally yielding radiative properties for aerosol mixture classifications used in AC-TC. Aerosol extinction is provided at 355 nm, and so for each aerosol mixture the ratio $\beta_{\text{aero}}(\lambda) / \beta_{\text{aero}}(0.355 \mu\text{m})$ at each λ is computed and then averaged spectrally using the same weightings as for cloud radiative properties as described below.
205

Aerosol scattering phase functions, as needed by the 3D RT codes, are represented by the Henyey-Greenstein (1941) function, which is given by

$$p_{HG}(\mu; g_{\text{aero}}) = \frac{1 - g_{\text{aero}}^2}{(1 + g_{\text{aero}}^2 - 2g_{\text{aero}}\mu)^{3/2}}, \quad (4)$$

satisfies

$$g_{\text{aero}} = \frac{1}{2} \int_{-1}^1 p_{HG}(\mu; g_{\text{aero}}) \mu d\mu, \quad (5)$$

210 and is used directly in the models (i.e., no need for tabulation). Owing to the size and irregularity of aerosol particles, and retrieval uncertainties, use of (4) is reasonable.

4.1.3. Liquid clouds

The standard version of RRTMG uses Hu and Stamnes's (1993) parametrizations of spectral β , ω_0 , and g for liquid droplets. For EarthCARE, however, these have been replaced by more precise Lorenz-Mie calculations tabulated for ranges of droplet effective radii r_{eff} and effective variances v_{eff} , which are defined, respectively, as

$$r_{\text{eff}} = \frac{\int_0^\infty n(r) r^3 dr}{\int_0^\infty n(r) r^2 dr} = \frac{\langle r^3 \rangle}{\langle r^2 \rangle}, \quad (6)$$

and

$$v_{\text{eff}} = \frac{\int_0^\infty (r - r_{\text{eff}})^2 n(r) r^2 dr}{r_{\text{eff}}^2 \int_0^\infty n(r) r^2 dr} = \frac{\langle r^2 \rangle \langle r^4 \rangle}{\langle r^3 \rangle^2} - 1, \quad (7)$$

where r is droplet radius. Droplet size distributions $n(r)$ are assumed (Chýlek et al. 1992) to be

$$220 \quad n(r) = \frac{N}{\Gamma(\nu)} \left(\frac{\nu}{\langle r \rangle} \right)^\nu r^{\nu-1} \exp\left(-\frac{\nu r}{\langle r \rangle}\right), \quad (8)$$

where $\langle r \rangle = \nu r_{\text{eff}} v_{\text{eff}}$ and $\nu = (1 - 2v_{\text{eff}})/v_{\text{eff}}$.

Lorenz-Mie computations (Wiscombe 1980), using Segelstein's (1981) refractive indices, were performed for r between 0.01 and 120 μm in increments of 0.05 μm , and for wavelengths λ between 0.25 and 100 μm in increments

of: 0.02 for $0.25 < \lambda < 2 \mu\text{m}$; 0.04 for $2 < \lambda < 3 \mu\text{m}$; 0.05 for $3 < \lambda < 10 \mu\text{m}$; 0.07 for $10 < \lambda < 20 \mu\text{m}$; and 0.1 for $20 < \lambda < 100 \mu\text{m}$. Phase functions and optical properties were integrated over RRTMG's spectral intervals for combinations of r_{eff} and ν_{eff} : r_{eff} from 0.5 - 40 μm in increments of 0.5 μm ; and ν_{eff} from 0.02 - 0.4 in increments of 0.02 μm . Spectral weightings for SW bands are the mean of downwelling irradiances at the tropopause and surface as predicted by a *line-by-line* RT model (Iacono et al. 2008) for the tropical atmosphere at solar zenith angle $\theta_0 = 0^\circ$. For LW bands, weightings are the Planck function at 275 K. In the RT models, values of r_{eff} and ν_{eff} are rounded to the nearest value in the table, which usually results in errors for β , ω_0 , and g of less than $\pm 1\%$.

As the 3D RT models are Monte Carlo solutions, they use normalized tabulated scattering phase functions $p(\mu)$ for droplets. Broadband, spectrally-integrated $p(\mu)$ have 1,800 equal angular bins, and their cumulative sums, as functions of μ , were computed by

$$R(\mu_s) = \frac{1}{2} \int_{\mu_s}^1 p(\mu) d\mu, \quad (9)$$

where μ_s is cosine of scattering angle, with $R(\mu_s = 1) = 0$ (forescatter) and $R(\mu_s = -1) = 1$ (backscatter). For efficiency, tables of μ_s were constructed for 1800 equally spaced values of R ; when a scattering event occurs, a uniform pseudo-random number gets generated $R \in [0,1]$, and linear interpolation sets μ_s , which is used to update a photon's direction cosines.

4.1.4. Ice clouds

Values of β , ω_0 , g , and scattering phase functions for ice clouds are based on Yang et al.'s (2013) theoretical functions for 11 crystal habits: droxtals, prolate spheroids, oblate spheroids, solid columns, hollow columns, aggregates composed of 8 solid columns, hexagonal plates, small aggregates composed of 5 plates, large aggregates composed of 10 plates, solid bullet rosettes, and hollow bullet rosettes. Maximum dimension for each habit ranges from 2 μm to 10,000 μm for 189 discrete sizes. Three surface roughness conditions were considered for each ice

245 habit: smooth, moderate, and severe. Each constituent has volume, projected area, effective size, extinction efficiency, ω_0 , and g . Their scattering phase functions are tabulated at 498 unequal angles, but were transformed into 1,800 equal angular bins for use in (9).

To make this dataset's size suitable for operational use, optical properties were averaged over λ and assumed distributions of habit, size, and roughness that were derived from CALIPSO observations (Baum et al. 2011). Resulting
250 phase functions and optical properties are functions of effective diameter which is defined as

$$d_{\text{eff}} = \frac{3}{2} \frac{\sum_i \int V_i(D) n(D) f_i(D) dD}{\sum_i \int A_i(D) n(D) f_i(D) dD}, \quad (10)$$

where V , A , and D are geometric volume, orientation-averaged projected area, and maximum dimension of ice
255 particle, respectively. $n(D)$ denotes crystal size distribution, and f_i indicates the percentage of each ice particle habit
and roughness. Values of d_{eff} range from 10 μm to 120 μm in increments of 5 μm . Band-averaged optical properties
were computed using the same weightings as in (10) while also weighting for spectral irradiance and then integrating
260 over RRTMG's spectral intervals. Spectral weight for SW bands was the TOA spectrum while for the LW it was the
Planck function at 250 K (per. comm., B. Yi, 2013).

4.1.5. Solid hydrometeors and rain

Solid hydrometeors are retrieved as though they were ice cloud, and their optical properties appear as such. In addition to liquid cloud properties, however, ACM-CAP reports layer rain rates R (mm h^{-1}). Raindrop size distributions
260 are assumed to follow Ulbrich's (1983) gamma distribution. Spectrally-integrated single-scattering properties are
defined using the same spectral weights as discussed in section 4.1.3 in conjunction with Mie scattering properties
for droplet radii between 10 μm and 2000 μm ; larger drops tend to break-up (e.g., Cotton and Gokhale 1967). Tables
of optical properties range from $R = 0.5 \text{ mm h}^{-1}$ to 50 mm h^{-1} in increments of 0.5 mm h^{-1} . *Figure 4a* shows rain drop
265 size distributions for three values of R for Ulbrich's (1983) formulation using $\mu = 0.056R - 0.74102$ (NB. This
 μ follows Ulbrich's Eq.2 and differs from μ used elsewhere in this paper). *Figure 4b* shows corresponding drop

effective radius and variance; note that as rain intensity increases, V_{eff} decreases, droplet spectrum narrows, and with this format, Marshall and Palmer's (1948) distribution occurs near $R = 13 \text{ mm h}^{-1}$, which is, by most standards, fairly heavy rain.

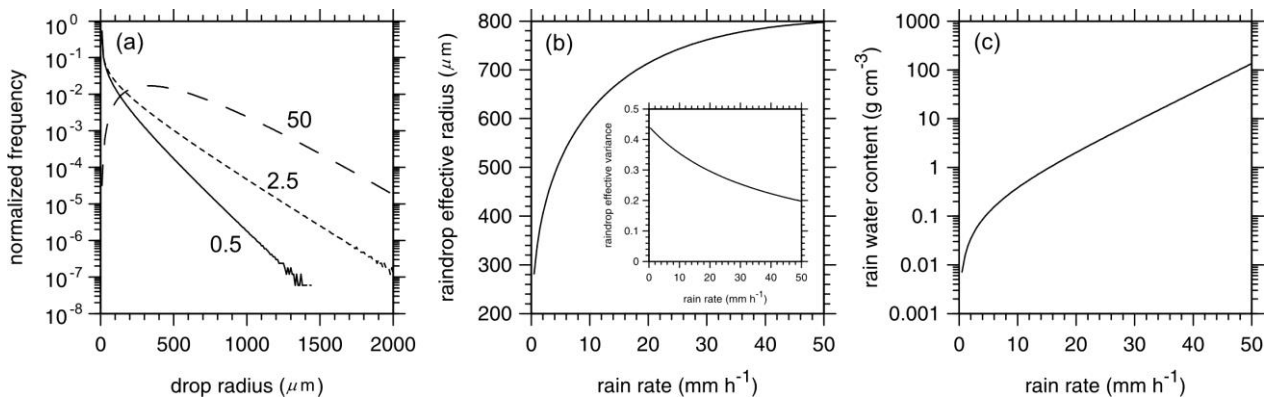


Figure 4: (a) Raindrop size distributions for three values of rain rate (mm/h). (b) Rain droplet effective radius and variance as functions of rain rate according to Ulbrich's (1983) formulation and the assumed gamma distribution parameter as discussed in section 4.1.5. (c) Rain water content as a function of rain rate.

270 The Mie phase functions that follow from *Figure 4* and (8) have very pronounced forward peaks that are difficult to capture well in the MC models. Hence, because rain usually resides beneath thick clouds where radiance fields are highly diffuse, the 3D RT models use $p_{HG}(\mu; g)$.

4.2. Optical properties: Underlying surfaces

280 Snow-free surface albedo over land for visible (0.3-0.7 μm) and infrared (0.7-5.0 μm) SW bands were calculated from climatological bidirectional reflection distribution function parameters for 16-day periods based on 12 years (2002-2013) of MODIS MCD43GF data (Schaaf et al. 2002). Terrestrial snow albedo data for the same spectral bands are based on Moody et al. (2007) whose calculations were, in turn, based on five years (2000–2004) of climatological statistics of Northern Hemisphere white-sky albedos for 16 International Geosphere–Biosphere Program (IGBP) ecosystem classes when accompanied by the presence of snow on ground. For ice-covered land or water surfaces, BB averaged albedos over 16,000 - 50,000 cm^{-1} are provided by X-MET (via ECMWF).

Ideally, the 3D RT models should include bidirectional reflection and emission functions; such as Rahman et al.'s (1993) land surface model, which is in EarthCARE's SW 3D RT code but global parameters are too lacking. Hence, spectral albedos, as just described, and the Lambertian assumption are used.

For open water surfaces, spectrally-independent ocean albedo is approximated by

$$290 \quad \alpha_{sfc} = 0.021 + x^2 \left(0.0421 + x \left(0.128 + x \left(-0.04 + x \left(\frac{3.12}{5.68+w} \right) + \frac{0.074x^2}{1+3w} \right) \right) \right), \quad (11)$$

where $x = 1 - \cos \theta_i$, θ_i is zenith angle of an incident photon, and w is surface wind-speed (m s^{-1}) (Hansen et al. 1983). The 3D SW model uses (11) for all photons arriving at a water surface. Additionally, it uses Cox and Munk's (1956) ergodic wave model to describe the probability of a SW photon incident at the surface being reflected, with probability defined by (11), toward a BBR telescope. As such, simulated radiances capture some semblance of Sun-glint; the effects of which are tempered by EarthCARE's orbit (Illingworth et al. 2015).

295 While the 1D SW model uses (11), with θ_0 replacing θ_i , to describe direct-beam albedo, its diffuse-beam albedo is

$$\langle \alpha_{sfc} \rangle = 0.03815 + \frac{0.1486}{5.68+w} + \frac{0.0026}{1+3w}, \quad (12)$$

which is just the integral of (11) assuming isotropic irradiance, regardless of sky condition. Last, hemispheric spectral emissivities for land and sea surfaces, for each RRTMG_LW band, are based on Huang et al. (2016). Like 300 albedo, emissivity is assumed to be Lambertian.

4.3. 1D radiative transfer modelling

The 1D RT models in RRTMG are meant to be applied to layered atmospheres with optical properties varying only in the vertical. As RRTMG was designed for use in large-scale models, it comes with algorithms that address unresolved horizontal fluctuations in cloud water content and cloud overlap. These algorithms are not needed for Earth-305 CARE because RRTMG will be applied to individual JSG columns resolved at ~ 1 km resolution with homogeneous layers.

The LW transport solver in RRTMG performs flux calculations for a single diffusivity angle with an adjustment for profiles that contain large H₂O vapour contents. It is an emissivity model that neglects scattering by all atmospheric constituents. Its SW solver employs the multi-layer delta-Eddington two-stream approximation (Wiscombe 1977), 310 which accounts for multiple scattering but, as with the LW solver, has well-documented conditional limitations for aerosol and cloud conditions (e.g., Li and Ramaswamy 1996; Barker et al. 2015a). Nevertheless, due to RRTMG's widespread use at the time of writing, it is used for EarthCARE with a minimum of alterations so as to be consistent with other current applications.

There are three applications of the 1D SW and LW RT models to each valid JSG column along the retrieved cross-section. The first, denoted as “all-sky”, uses the full retrieved profiles. Second is “clear-sky” where clouds are removed leaving molecules and aerosols. The third application is “pristine-sky” in which clouds and aerosols are removed leaving just the molecular atmosphere. 315

4.4. 3D radiative transfer modelling

Monte Carlo solutions of the 3D RT equation are used to calculate both SW and LW fluxes and radiances. This 320 represents a break from, and advancement over, previous satellite missions that have been limited to use of 1D RT solvers. The 3D RT models are discussed in the following subsections.

4.4.1. SW radiation

Solar fluxes and radiances are computed by a local estimation-based Monte Carlo algorithm (Marchuk et al. 1980; Barker et al. 2003). It is discussed here in general terms, except for aspects that have not been published or were 325 designed specifically for EarthCARE.

Unlike the 1D RT models that act on individual columns, 3D RT models require collections of columns. Photons get injected uniformly across D^+ that are expected to be at most ~60 km along-track by ~30 km across track (see *Figure 2*). Cosine of solar zenith angle μ_0 is uniform over D^+ and set by its central pixel. Total numbers of injected photons per domain are to be determined, as they depend on computational resources, acceptable Monte Carlo 330 sampling noise for either fluxes or radiances, and areal extents of individual D^+ . Number of photons injected per spectral band is proportional to the weight associated with quadrature points in RRTMG's CKD model.

Each atmospheric cell has a spectral cumulative extinction vector whose entries for attenuating constituents are ordered, for efficiency, as: ice cloud; liquid cloud; Rayleigh scatterers; absorbing gases; aerosols; and rain. When an interaction between an attenuator and a photon takes place, a uniform random number between 0 and 1 is generated, 335 the (normalized) extinction vector is searched sequentially thus setting the attenuator, with its single-scattering properties used to establish whether absorption or scattering takes place (cf. Barker et al. 2003). When a scattering event occurs, a fraction $1 - \omega_0$ of the photon's weight goes into local heating. What remains has its weight reduced by a factor ω_0 .

At each scattering event, the probability of photons being redirected toward a BBR telescope is determined using 340 $p(\mu)$. Transmittance through total optical depth between scattering event and satellite sets the probability of scattered photons reaching the satellite; as this distance is large and the telescope's aperture small, any path deviation is assumed to result in undetected photons. These contributions are summed to produce final estimates of BBR radiances.

The local estimation method runs into trouble when photons travelling directly toward a telescope undergo a scattering event by cloud particles whose $p(\mu)$ have sharp diffraction peaks (Iwabuchi 2006). Such rare contributions are 345 valid, but they catastrophically elevate uncertainties, which are difficult to counter with large numbers of "typical" contributions when number of injected photons is small, as for EarthCARE. A simple way to help, without impacting fluxes and HRs, is to use the tabulated exact $p(\mu)$ to determine all photon forward trajectories but only those radiance contributions from the first N_{Mie} scattering events by cloud particles. Thereafter, the blunt-nosed 350 $p_{HG}(\mu; g)$ is used to compute radiance contributions (see Barker et al. 2003).

The rationale behind this approximation is that low-order scatterings that contribute to BBR radiances come largely from $p(\mu < 0)$, and because they do not spike radiances, several of them are allowed so as to capture details of 355 $p(\mu)$. For optically thin clouds there will be few scattering events and so calls to $p_{HG}(\mu; g)$ will be rare. For thicker clouds, however, after ~ 3 scatterings photons will have had a fair chance of being redirected onto upward

355 travelling trajectories that can spike radiances. EarthCARE uses $N_{\text{Mie}} = 4$ for, as shown in section 5.2, it strikes a balance between bias and random radiance errors (Barker et al. 2003).

When a photon arrives at the surface, it undergoes Lambertian reflection for albedo α_s with $1 - \alpha_s$ of its weight removed and added to *net* surface irradiance. The probability of being reflected toward a BBR sensor goes according to Lambertian for land, ice and snow, and Cox and Munk (1956) for open water (see section 4.2).

360 A unique, memory saving, aspect of EarthCARE's SW and LW 3D RT models is that the 3D atmosphere never appears explicitly in them. This is because all columns in D^+ exist along the retrieved cross-section; optical properties of columns off this plane come from a *donor* column in it, as dictated by ACMB-3D's scene construction algorithm (Barker et al. 2011; Qu et al. 2023).

4.4.2. LW radiation

365 Longwave radiances are computed efficiently with the backward Monte Carlo technique (Walters and Buckius 1992; Modest 2003). Cole's (2005) implementation is used for EarthCARE. Much of the code resembles that of the SW Monte Carlo, and so discussion is focused on its unique aspects.

Unlike the SW Monte Carlo, photons are not injected uniformly onto the top of D^+ since the domain itself is the source. Rather, reciprocity of paths from an emission source to a sensor is assumed to hold (Case 1957). Hence, 370 photons trace back from the top of the assessment domain to their source of emission where the contribution to radiance is computed using local temperature and optical properties. This process is repeated for each point in the assessment domain and radiance view angle. To reduce the number of rays traced, which is often the main computational expense, rather than trace a unique ray for each quadrature point in the CKD model it is assumed that scattering optical properties are the same for all quadrature points in a single wavelength interval.

375 For a given wavelength interval in the CKD model a band-representative photon path is traced backward from the top of the domain to determine a scattering path that can be related to each photon injected for each quadrature point in the band. The photon travels straight through the domain until it has accumulated sufficient scattering optical depth to scatter in the atmosphere or scatter due to an interaction with the surface. Scatter within the atmosphere is determined based on the cumulative distribution of scattering extinction; similar to that in the SW algorithm. For each

380 quadrature point in CKD wavelength interval a random number is determined which sets the optical depth that must be accumulated to have an absorption event. Absorption optical depth is accumulated along the path until the photon undergoes an absorption event at which point $(1 - \omega_0)B(T)$ is added to the radiance, where $B(T)$ is integrated Planck function, and T is temperature. If, however, the photon reaches the surface, a uniform random number is used to determine if there is absorption by the surface. If the random number is less than surface emissivity ε the radiance
 385 is incremented by $B(T_s)$, where T_s is the surface temperature. Otherwise, the path is reflected.

Upward thermal flux at a, potentially variable, reference height is also computed. This is done using a method similar to that used for radiances. The main difference being the selection (i.e., random generation) of the direction of each ray injected into the domain from the reference height. Once the ray direction is selected, accumulation of emission contributions is the same as it is for radiances.

390 **4.4.3. Estimation of Monte Carlo uncertainty**

For a fixed domain, 1D RT models produce single deterministic solutions. Monte Carlo algorithms, however, yield a sample from a distribution. In general, the breadth of the distribution, or Monte Carlo uncertainty, depends on the number of injected photons, the variable being diagnosed, and the geometric and optical properties of the field.

Monte Carlo uncertainties are estimated by explicitly producing M samples of a random variable x , each using N_s
 395 photons and initialized with a unique, uniformly distributed, random number. Estimated population mean is simply

$$\hat{\mu}_x(M, N_s) = \frac{1}{M} \sum_{m=1}^M x(m, N_s), \quad (13)$$

where $x(m, N_s)$ is the m^{th} realization of x . From the central limit theorem,

$$\lim_{M \rightarrow \infty} p \left[\left| \frac{\hat{\mu}_x(M, N_s) - \mu_x}{\sigma_x(M, N_s)} \right| \leq a \right] = \frac{1}{\sqrt{2\pi}} \int_{-a}^a e^{-u^2/2} du, \quad (14)$$

where μ_x and σ_x are mean and standard deviation of the population from which samples are drawn. Letting
 400 $\hat{\sigma}_x(M, N_s)$ be an estimate of σ_x based on M samples, Monte Carlo “uncertainty” is defined as one standard deviation under a Gaussian distribution of samples. This amounts to setting $a = 1$ in (14), and implies that after M realizations, $\hat{\mu}_x$ has a 68% chance of lying in

$$\left[\hat{\mu}_x(M, N_s) - \frac{\hat{\sigma}_x(M, N_s)}{\sqrt{M}}, \hat{\mu}_x(M, N_s) + \frac{\hat{\sigma}_x(M, N_s)}{\sqrt{M}} \right], \quad (15)$$

making for an uncertainty of

$$405 \quad \hat{\rho}_x(M, N_s) \approx \pm \frac{\hat{\sigma}_x(M, N_s)}{\sqrt{M}}. \quad (16)$$

As M increases, estimates of $\hat{\sigma}_x$ stabilize; they do not go to zero.

5. Results

This section’s main purpose is to showcase a sample of EarthCARE’s radiation products; some of which get utilized directly for radiative closure assessment as will be reported in a later study. Results are shown using only ACM-CAP
 410 data; corresponding results for ACM-COM’s composites are qualitatively the same. Results are shown mainly using data from two test frames: the “Halifax frame”, which passes near Halifax, Canada; and the “Hawaii frame”, which passes near Hawaii (Qu et al., 2023).

As noted in the Introduction, many radiative quantities are averaged over ~ 100 km 2 assessment domains. It is expected that these domains will be configured to 21 km along-track by 5 km across-track. This is to strike a balance
 415 for closure assessment between limiting the scene construction algorithm’s (Qu et al. 2023) impact on radiance and flux estimates, yet facilitating horizontal transport of photons. To simplify presentation of results, radiative transfer estimates are shown for a reference height of 20 km (cf. Loeb et al, 2002); in operations they will vary.

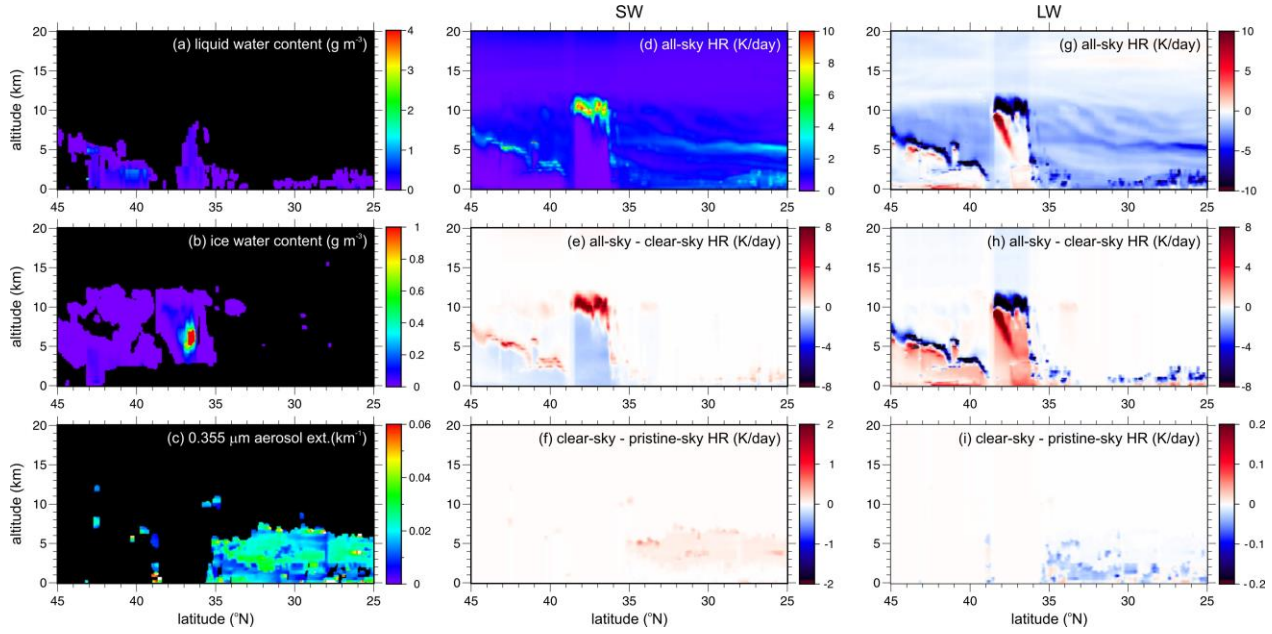


Figure 5: (a) Profiles of domain-average cloud liquid water content, (b) ice water content, and (c) aerosol extinction coefficient for 21 km-long assessment domains, for the *Halifax* frame, as inferred by ACM-CAP's synergistic algorithm. (d) Corresponding domain-average, all-sky SW broadband heating rates computed by RRTMG's 1D RT model. (e) Difference between HRs shown in (d) and those computed by RRTMG for clear-sky conditions. (f) As in (e) except these HR differences are for clear-skies and pristine-skies. (g), (h), and (i) are as in (d), (e), and (f), respectively, except these are for LW broadband heating rates.

420
425

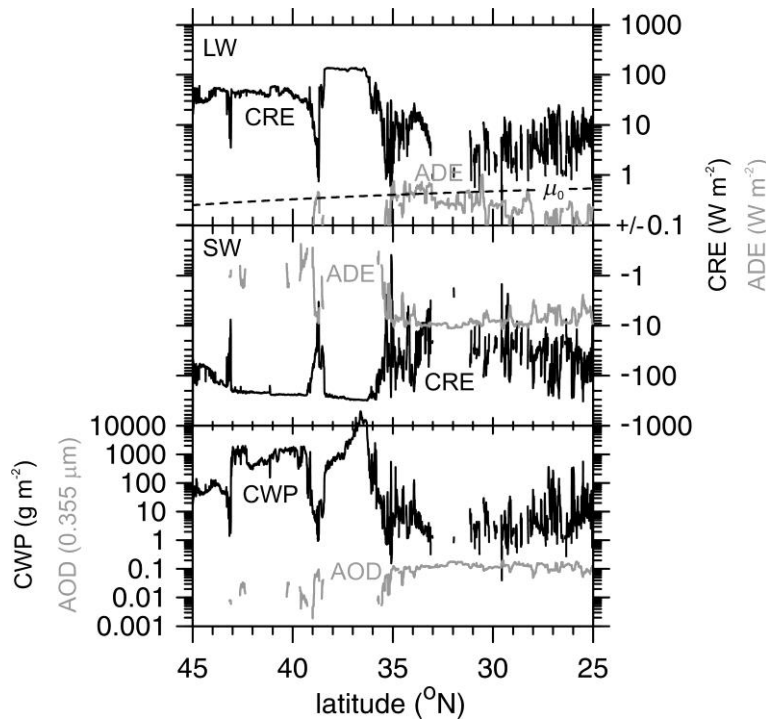
5.1. RRTMG 1D fluxes: Pristine-, clear-, and all-sky

As discussed in section 2, broadband flux and heating rate profiles for all admissible L2 columns are computed by RRTMG's SW and LW 1D RT models. The left column of *Figure 5* shows ~2,200 km of cloud and aerosol properties retrieved by ACM-CAP's synergistic algorithm (Mason et al. 2023). These results pertain to 21 km-long non-overlapping assessment domains near the central of the *Halifax* test frame. The middle column shows corresponding SW all-sky HRs and differences between all-sky HRs and clear-sky HRs (cloud radiative effect: CRE), and clear-sky HRs and pristine-sky HRs (aerosol direct effect: ADE). Aside from the usual 1D RT features, such as large SW heating near cloudtop and much smaller values below relative to clear-sky, the only peculiarity is the fairly strong heating at ~5 km altitude in the south-end. This is due to an elevated layer of water vapour. The vast majority of minor heating due to aerosol is from continental pollution that overrides sea salt.

The rightmost column in *Figure 5* is like the middle column but it shows results for LW HRs. As expected, there is strong cooling in the upper 1 - 2 km, or so, of clouds, little net heating or cooling below, and general cooling from

cloudless-skies. LW CREs are generally stronger than in the SW and exhibit strong cooling near all cloudtops and
440 warming in clouds, when they are of sufficient vertical extent. LW ADEs are an order of magnitude smaller than their SW counterparts, and manifest themselves as cooling just beneath their SW warming counterparts.

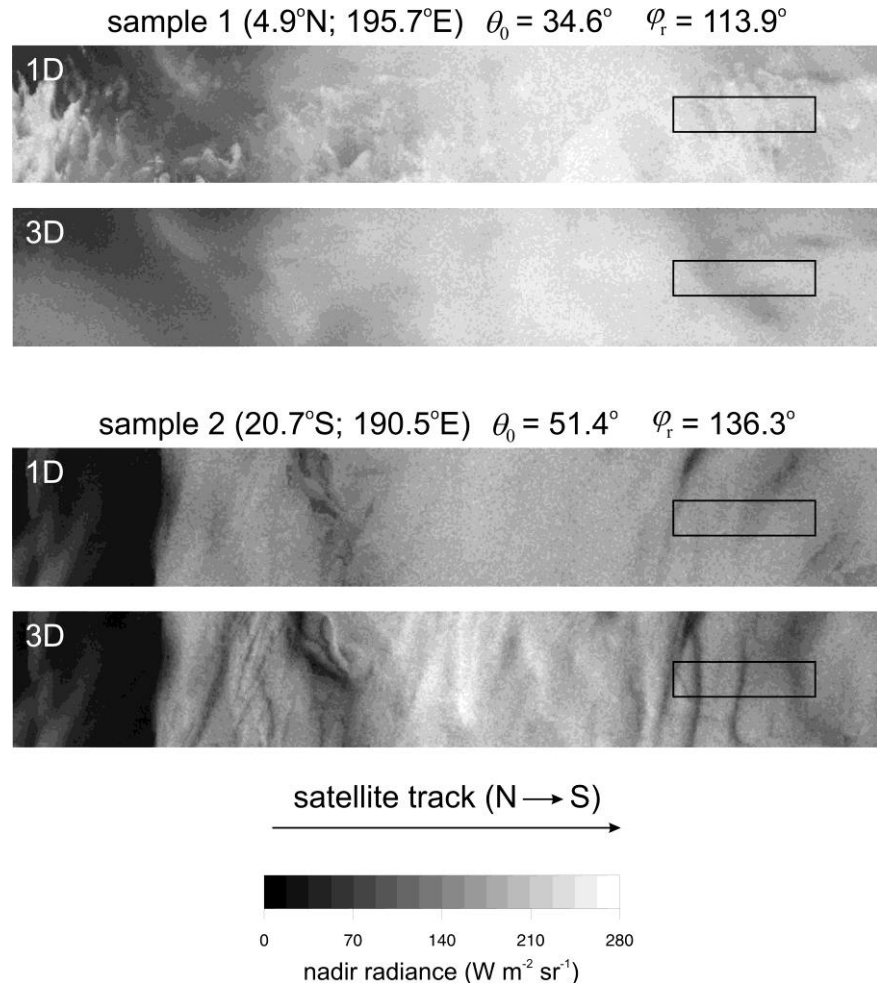
To demonstrate what will be available in the ACM-RT archive, *Figure 6* shows TOA CRE, ADE, and some integrated cloud and aerosol properties that correspond with *Figure 5*. Some noteworthy points here are SW CRE reaching
445 $\sim 300 \text{ W m}^{-2}$ at $\mu_0 \approx 0.3$ due to clouds near 41°N with large cloud water paths (CWP), LW CRE reaching 100 W m^{-2} near 37°N due to supercooled liquid aloft, and weak ADE ($\sim -10 \text{ W m}^{-2}$ in the SW and less than 1 in the LW)
stemming from aerosol optical depth, at $0.355 \text{ }\mu\text{m}$, being at most 0.2. Aside from this, there is very little to comment
on in these plots; they serve to demonstrate what will be available in the ACM-RT archive.



450 **Figure 6:** Top panel: Cloud radiative effect (CRE) and aerosol direct effect (ADE) as functions of latitude for broadband SW at an altitude of 20 km for 21 km-long assessment domains as shown in *Figure 5*. μ_0 is cosine of solar zenith angle. Middle panel: As in top panel except it is for broadband LW. Lower panel: Assessment domain-average cloud water path (CWP) and aerosol optical depth (AOD).

455 5.2. On the benefits of employing 3D RT models

As mentioned above, one of EarthCARE's notable advancements over prior like-missions is operational use of both 1D *and* 3D RT models. The decision to use 3D RT models was fuelled by myriad studies that show systematic differences between 1D and 3D treatments of RT, especially for cloudy atmospheres at solar wavelengths. Results shown in this subsection help justify the computational expensive of using 3D RT models operationally.



460

Figure 7: Nadir broadband SW radiances for two sample regions in the Hawaii frame; both regions measure 128 km along-track by 20.25 km across-track. Small rectangles indicate a 5 x 21 km assessment domain, the size used for radiative closure assessments. Central values of latitude and longitude are listed along with θ_0 and φ_r (measured clockwise from the satellite's tracking direction). Labels 3D and 1D indicate RT model dimensionality using horizontal grid-spacings of 0.25 km and 10^6 km.

465

Before getting to results that apply strictly to EarthCARE, consider a detailed view of the impact of neglecting multi-dimensional RT. *Figure 7* shows nadir SW radiances simulated by a Monte Carlo RT model (Villefranque et al.

2019) for two stretches of the *Hawaii* test frame, each measuring 128 km along-track by 20.25 km across-track (Qu
 470 et al. 2023). The 3D RT simulation used horizontal grid-spacing $\Delta x = 0.25$ km while its 1D rendition used Δx set
 arbitrarily large. Hence, differences in their radiances stem entirely from the dimensionality of the RT solution. For
 this demonstration, the number of photons per column was 4,096, which is, on an areal density-basis, several times
 larger than what will be used operational for the EarthCARE mission.

These images display the varied and complicated ramifications on radiances when 1D RT modelling theory is as-
 475 sumed to apply. For sample 1, 1D radiances show much variability and sharp contrasts relative to their 3D counter-
 parts; off-nadir views (not shown) look much the same. This region is blanketed by thick overcast ice cloud, which at
 $\Delta x = 0.25$ km, act to diffuse upwelling radiation, thus blurring localized reflection from low-level intermittent
 liquid clouds (e.g., Diner and Martonchik 1984). When 1D RT is affected by setting Δx large, however, flow of
 radiation is confined to the vertical and the sharp features of liquid clouds remain intact regardless of altitude.

480 On the other hand, sample 2 has mostly low-to-mid-level liquid clouds and shows, due in part to large θ_0 , the more
 familiar differences between 3D and 1D RT (e.g., Barker et al. 2017). In particular, 1D radiances lack texture, whilst
 their 3D counterparts exhibit much contrast due to shadowing and cloud-side illumination. Note, however, that
 imagery for thin liquid clouds at the northern edge of the sample depend little on Δx . This is because reflected
 photons undergo small numbers of scattering events and thus tend to exit clouds close to where they enter.

485

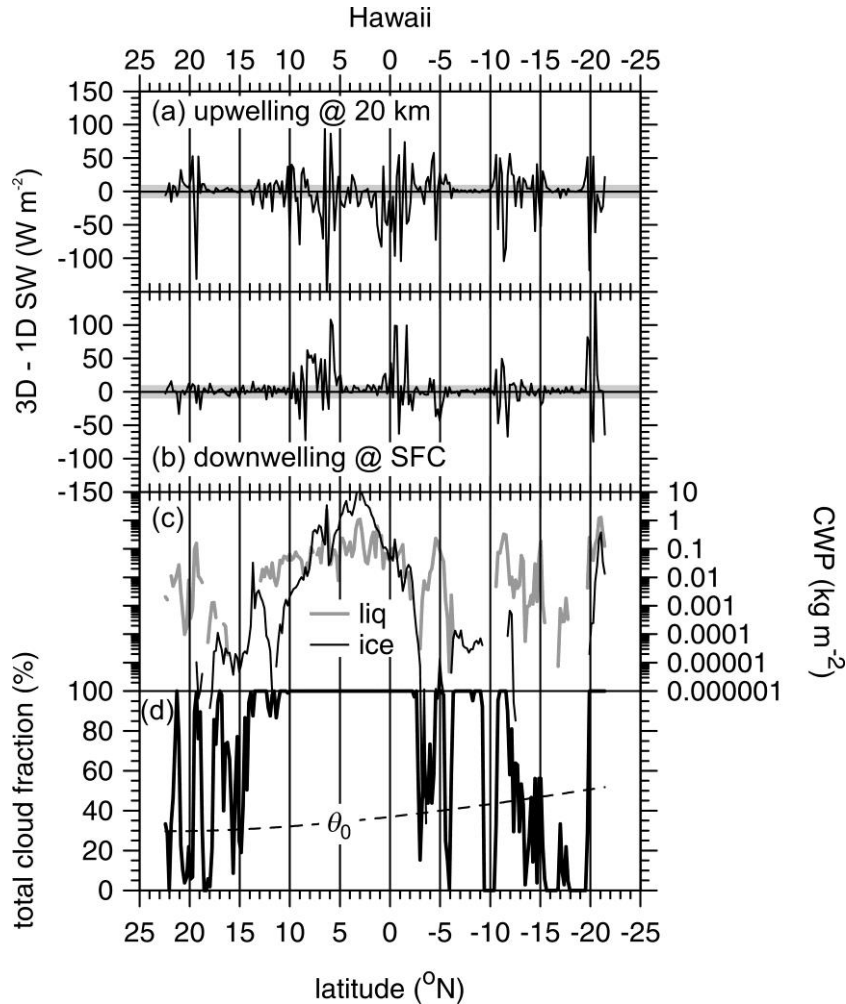


Figure 8: (a) Difference between upwelling SW fluxes at an altitude of 20 km as predicted by 3D and 1D RT models for 5×21 km assessment domains of the Hawaii frame. Shaded area indicates EarthCARE's goal of $\pm 10 \text{ W m}^{-2}$. (b) As in (a) except this is for SW surface irradiance. (c) Mean liquid and ice cloud water paths for the Hawaii frame's 5×21 km domains. (d) Corresponding total cloud fraction and solar zenith angle for the same assessment domains.

490

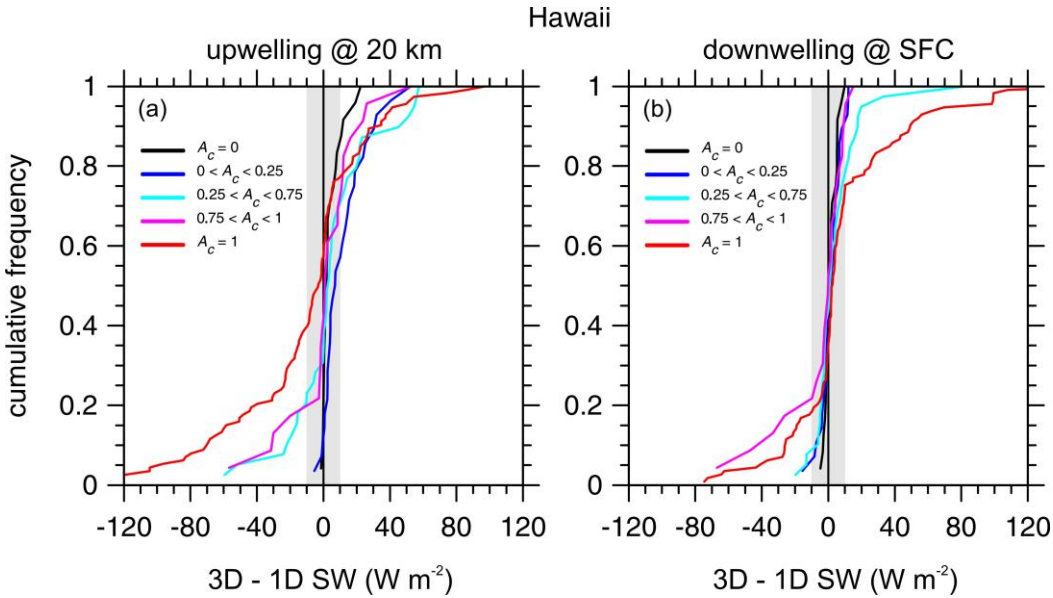
495

Consider now differences one can encounter in applications to EarthCARE retrievals. *Figure 8* shows differences between 3D and 1D RT modelled SW broadband upwelling fluxes at 20 km and surface irradiances for 5×21 km assessment domains across the *Hawaii* frame using ACM-CAP cloud properties. Values for 3D and 1D RT are from the Monte Carlo model using $\Delta x = 1 \text{ km}$ and arbitrarily large Δx , respectively. Each simulation used 2.5×10^6 photons, which is likely much larger than what will be used operationally throughout the mission. For almost cloud-free skies, thin ice cloud-only with ice water path $\text{IWP} < 0.01 \text{ kg m}^{-2}$, and very thick clouds with $\text{CWP} > 0.5 \text{ kg m}^{-2}$, differences are well within $\pm 10 \text{ W m}^{-2}$ for fluxes at both levels. Clearly, under these conditions SW photon trajec-

ries are characterized by either extremely small or large numbers of scattering events with cloud particles for both 1D
500 and 3D RT. For the majority of other cloud conditions, however, especially with CWP in the vicinity of $\sim 0.1 \text{ kg m}^{-2}$, differences can be much larger than $\pm 30 \text{ W m}^{-2}$, which far exceeds EarthCARE's goal (ESA 2001; Illingworth et al. 2015; Eisinger et al. 2023). The implication being that many attempts to perform a radiative closure assessment on EarthCARE's retrievals will be doomed to failure if 1D RT models are adhered to.

Figure 9 shows cumulative frequency distributions of the differences shown in Figure 8 for several ranges of total
505 cloud fraction A_c . For upwelling fluxes at 20 km with $A_c < 0.25$, median differences are all close to zero. The same goes for 3D - 1D mean-bias errors (MBEs) as listed in Table 2. Differences tend to be distributed more or less symmetrically about zero with occasional large differences, exceeding $\pm 50 \text{ W m}^{-2}$, enhancing root mean-square errors (RMSEs) as A_c increases (see Table 2) relative to the 16- and 84-percentiles of the distributions, which can be gleaned from the graphs.

510 There are at least two interesting points to these plots that involve extremal cloud conditions. First, 3D - 1D can be expected to be maximized for overcast domains, which implies that the geometry of overcast clouds is often anything but approximately plane-parallel and homogeneous (cf. Hogan et al. 2019). Second, for assessment domains D with $A_c = 0$, 3D - 1D values for upwelling flux at 20 km show a tendency to be positive on account of contributions from clouds in the surrounding buffer-zone (see Figure 2).



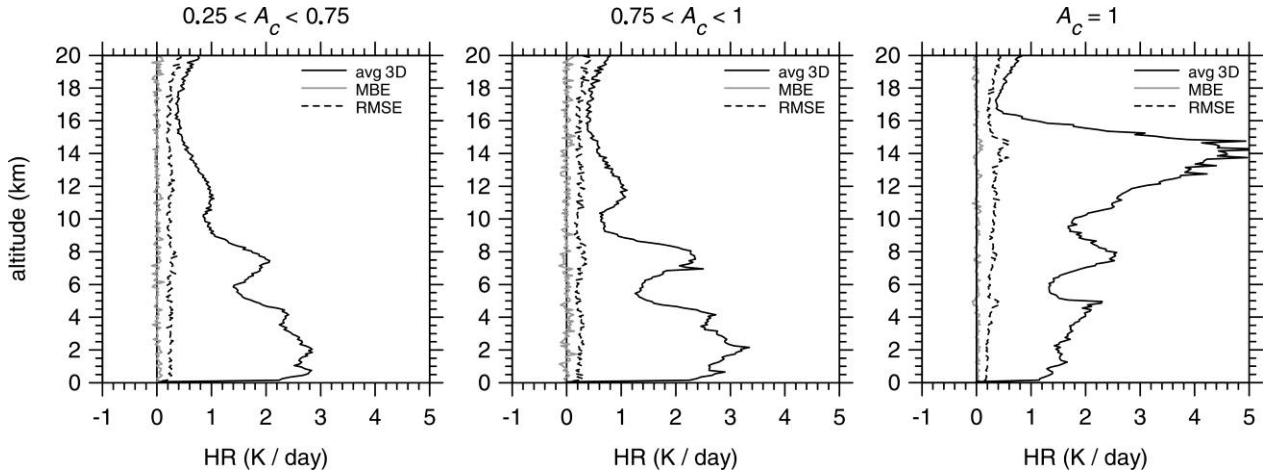
515

Figure 9: (a) Cumulative frequency distributions for differences between 3D and 1D Monte Carlo RT model estimates of upwelling SW flux at an altitude of 20 km for 5×21 km assessment domains for the Hawaii frame partitioned according to assessment domain total cloud fraction A_c (see Table 2 and Figure 8). Shaded area indicates EarthCARE's goal of $\pm 10 \text{ W m}^{-2}$. (b) As in (a) except these are for surface (SFC) irradiances.

520

Table 2: Mean 3D SW RT values, mean bias errors (MBEs), and root mean-square errors (RMSEs) for corresponding 3D - 1D RT results (see Figure 8 and Figure 9) for 5×21 km assessment domains for the Hawaii frame and several ranges of total cloud fraction A_c .

total cld frac	cases	upwelling flux at 20 km (W m ⁻²)			SFC irradiance (W m ⁻²)		
		3D RT	MBE	RMSE	3D RT	MBE	RMSE
$A_c = 0$	24	81.0	4.2	6.2	698.0	1.5	3.6
$0 < A_c < 0.25$	28	93.5	12.2	13.8	780.0	1.5	6.3
$0.25 < A_c < 0.75$	39	112.0	5.0	25.2	755.9	4.6	16.1
$0.75 < A_c < 1$	23	128.0	1.3	21.6	777.0	-5.6	19.7
$A_c = 1$	113	395.5	-11.5	41.8	462.7	8.6	35.2



525

Figure 10: Mean 3D RT SW heating rate (HR) profiles for 5×21 km assessment domains for the Hawaii frame partitioned according to assessment domain total cloud fraction A_c (see *Figure 8*). Also shown are mean bias errors (MBEs) and root mean-square errors (RMSEs) between 3D and 1D RT models. Numbers of cases per A_c range are listed in *Table 2*.

530

Figure 10 shows that SW HR differences between 3D and 1D RT for the *Hawaii* frame's 5×21 km assessment domains are much less dramatic than those seen in *Figure 8* and *Figure 9* for boundary fluxes. At all altitudes and ranges of A_c , MBEs are essentially zero and close in magnitude to Monte Carlo uncertainties for 2.5×10^6 photons. There are several reasons why RMSE values are ~ 10 x larger than Monte Carlo uncertainties, and only increase slightly as A_c increases. There are the obvious differences due to cloud side illumination, shadowing, and photon entrapment (Hogan et al. 2019), as well as impacts on flux profiles for 3D RT due to out-of-domain sources and sinks of photons; i.e., clouds outside D , but still in D^+ , that cast shadows or scatter radiation into D .

535

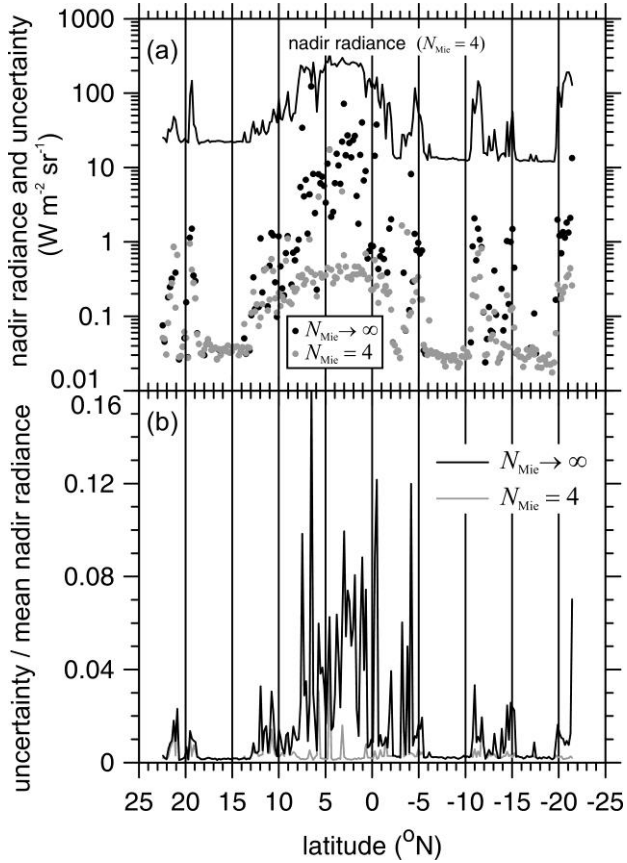


Figure 11: (a) Line is 3D RT nadir broadband radiances using $\Delta x = 1$ km when reverting to the Henyey-Greenstein phase function p_{HG} after $N_{\text{Mie}} = 4$ cloud particle scattering events for 5×21 km assessment domains of the Hawaii frame. Dots are Monte Carlo uncertainties when p_{HG} is never used ($N_{\text{Mie}} \rightarrow \infty$) and when it is used after 4 cloud scattering events ($N_{\text{Mie}} = 4$). (b) Using data in (a), Monte Carlo domain-average uncertainties relative to mean values for both values of N_{Mie} . Each domain received 2.5×10^6 photons.

540 There is the possibility that radiative closure assessments of cloud and aerosol retrievals could (i.e., should) use broadband radiances rather than fluxes. There are reasons both for and against this. For instance, off-nadir BBR radiances offer powerful assessments due to their weak correlation, relative to nadir BBR radiances, with MSI radiances that are used for some retrievals. They can, however, arise from attenuators outside the domain being assessed (see Barker et al 2015b). On the other hand, all of EarthCARE's performance goals are in terms of BBR fluxes, which will be estimated regularly by tailor-made algorithms (Velázquez-Blázquez et al. 2023a) despite adding, at times substantial, uncertainty at the last step of EarthCARE's processing chain.

Regardless, SW BBR radiances will be estimated throughout the mission. *Figure 11* shows nadir values for the *Hawaii* frame's assessment domains using 2.5×10^6 photons per assessment domain and $\Delta x = 1$ km. It also shows relative Monte Carlo uncertainties for $N_{\text{Mie}} = 4$ and $N_{\text{Mie}} \rightarrow \infty$. As 2.5×10^6 photons / domain is likely to be 555 more than routine operations can afford, uncertainties for $N_{\text{Mie}} \rightarrow \infty$ could be substantially larger than those shown here. This would render them useless for most assessments. While use of $N_{\text{Mie}} = 4$ will help, as is evident for the thick clouds between 0° to 10°N and near 20°S , it will foster errors in radiances themselves. Two options are being considered: i) use radiances, instead of fluxes, for assessments when their relative Monte Carlo uncertainties are less than some specified value (e.g., 0.01; see *Figure 11*); and ii) unbiased variance reduction methods (e.g., 560 Iwabuchi 2006).

As is well known, flux and radiance differences between 3D and 1D treatments of RT for LW radiation are usually much smaller than those for SW radiation (e.g., Ellingson and Takara 2005; Cole et al. 2005; Hogan et al. 2016; Fauchez et al. 2017). *Figure 12* shows the LW counterpart of the upper panel in *Figure 8*. When differences go beyond $\pm 10 \text{ W m}^{-2}$, they do so along with corresponding large differences in SW fluxes; typically for overcast skies 565 with CWP $\sim 0.1 \text{ kg m}^{-2}$. As shown in *Figure 13*, $\sim 5\%$ of overcast cases exhibit 3D fluxes that are less than their 1D counterparts by more than 10 W m^{-2} . For these domains, CWPs are small relative to their neighbouring domains. This demonstrates a difficulty when interpreting "fluxes" for 5×21 km domains: at 20 km altitude, fluxes for 3D 570 RT can be influenced substantially by adjacent cloudier domains. *Table 3*, however, shows that 3D and 1D fluxes usually differ by less than $\pm 1 \text{ W m}^{-2}$ which is on the order of the Monte Carlo uncertainty for these calculations, roughly 0.2 W m^{-2} .

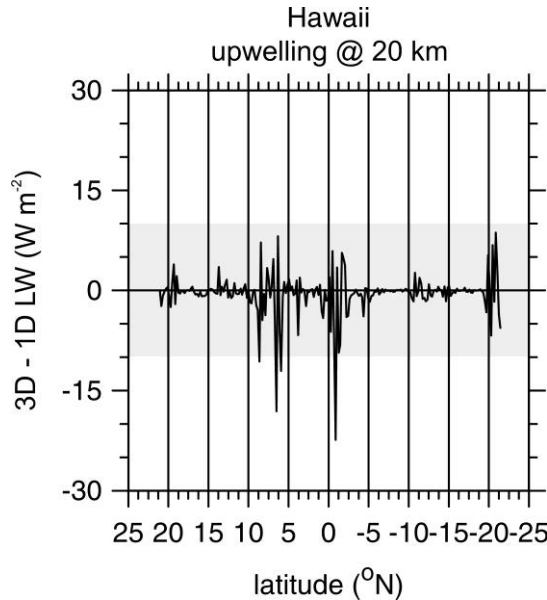


Figure 12: Difference between upwelling LW fluxes at an altitude of 20 km as predicted by 3D and 1D RT models for 5×21 km assessment domains of the Hawaii frame. A positive value means that 3D upwelling flux exceeds its 1D counterpart. Shaded area indicates EarthCARE's goal of $\pm 10 \text{ W m}^{-2}$.

575

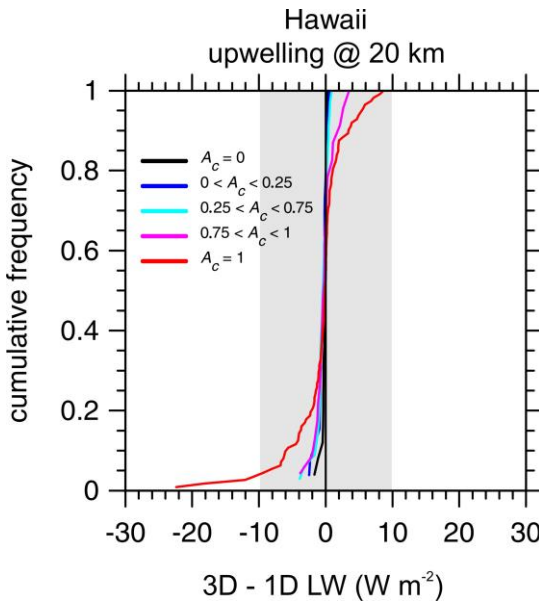


Figure 13: Cumulative frequency distributions for differences between 3D and 1D RT model estimates of upwelling LW flux at an altitude of 20 km for 5×21 km assessment domains for the Hawaii frame partitioned according to assessment domain total cloud fraction A_c (see Table 3). Shaded area indicates EarthCARE's goal of $\pm 10 \text{ W m}^{-2}$.

580

Table 3: Mean 3D LW RT values, mean bias errors (MBEs), and root mean-square errors (RMSEs) for corresponding 3D - 1D RT results (see *Figure 8* and *Figure 9*) for 5 x 21 km assessment domains for the Hawaii frame and several ranges of total cloud fraction A_c .

total cld frac	cases	upwelling flux at 20 km (W m ⁻²)			RMSE
		3D RT	MBE		
$A_c = 0$	25	285.4	-0.2	0.4	
$0 < A_c < 0.25$	26	289.2	-0.5	0.7	
$0.25 < A_c < 0.75$	34	286.0	-0.5	1.0	
$0.75 < A_c < 1$	23	287.5	-0.2	1.5	
$A_c = 1$	112	208.9	-0.7	4.3	

585 **6. Summary**

The EarthCARE satellite mission's objective is to retrieve profiles of aerosol and water cloud physical properties from measurements made by its cloud-profiling radar (CPR), backscattering lidar (ATLID), and passive multispectral spectral imager (MSI). While several L2a processes infer geophysical properties using measurements from a single sensor (see several articles in this special issue), EarthCARE's primary product comes from the L2b synergistic retrieval algorithm in ACM-CAP (Mason et al. 2023). These retrievals, together with other geophysical properties obtained either from pre-existing satellite data or real-time weather prediction models, are input into broadband (BB) radiative transfer (RT) models that predict radiances, and fluxes, commensurate with measurements made, and inferred from, EarthCARE's BB radiometer (BBR). The scientific goal is that modelled and "observed" BB fluxes differ, on average, by less than ± 10 W m⁻².

595 This report described the BB RT models used for EarthCARE and their products, which together comprise the ACM-RT process. Shortwave (SW) and longwave (LW) flux and heating rate (HR) profiles are computed by a 1D solver, based on RRTMG, for each ~1 km nadir column of inferred properties. In addition to the 1D RT models, which are ubiquitous to almost all operational and research satellite missions, EarthCARE is the first to employ 3D (Monte Carlo) RT models operationally. Both SW and LW models will compute radiances for the BBR's three viewing

600 directions, with the SW model also computing flux and HR profiles. The 3D LW model produces only upwelling fluxes at a variable reference level as dictated by the BMA-FLX process (Velázquez-Blázquez et al. 2023a). All 3D RT products are averages over 5×21 km “assessment domains” that are constructed in the ACMB-3D process (Barker et al. 2023) using a radiance mapping algorithm and MSI data (Barker et al. 2011).

When the ACM-CAP process runs successfully, its retrievals are operated on by the RT models. Failing this, the RT 605 models are applied to “composite” atmospheric profiles generated in the ACM-COM process by combining L2a retrievals from individual sensors. Usually, this involves filling grid-cells with retrievals from either CPR or ATLID data. When two L2a estimates exist for a cell, the one with the least relative uncertainty is selected. ACM-COM also prepares either ACM-CAP or composite atmospheres for use in RT models by bringing together information about atmospheric state and surface optical properties. Regardless of what atmosphere is used, nadir profiles are broadened 610 across-track by mapping indices from ACMB-3D in order to create 3D domains for the 3D RT models to use. A subset of ACM-RT’s products is passed forward to the ACMB-DF process where a “radiative closure assessment” executes in an attempt to quantify the likelihood that EarthCARE’s goal has been achieved.

615 Data from the EarthCARE test frames (Qu et al. 2023; Donovan et al. 2023) were used to demonstrate some of the products to be expected from ACM-COM and ACM-RT. In several respects, products associated with the 1D RT models resemble closely those available from the CloudSat mission (e.g., L’Ecuyer et al. 2008). The most notable extension is that ACM-RT will be reporting continuous cloud and aerosol radiative effects based on 3D RT model 620 results.

The majority of the results reported here (see section 5.2) had to do with the benefits expected from operational 625 application of 3D RT models. The ACM-RT process is the most computationally intensive one in EarthCARE’s processing chain. While a significant amount of computer time is required by both of the 1D RT models and 3D LW RT model, the lion’s share of ACM-RT’s allocated time is consumed (inevitably entirely) by the 3D SW RT model. Its voracity is such that only a portion of a frame’s available assessment domains will be operated on; the expectation is, however, that sufficient numbers of samples will be realized over the duration of the mission. This is because of the fairly large number of photons that have to be injected into the Monte Carlo RT model in order to produce flux and radiance estimates with uncertainties small enough to realize beneficial radiative closure assessments in the 625

ACMB-DF process (Barker et al. 2023). The most demanding product is off-nadir radiances. Finalization of exactly what the 3D RT models produce will be determined during EarthCARE’s commissioning phase.

If results presented in *Table 2* and *Figures 5* through *7* can be taken as representative, operational use of SW 3D RT modelling will be well-worth its heavy computational load. This is because differences between 3D and 1D RT
630 values of upwelling fluxes and radiances can be either positive or negative (cf. Hogan et al. 2019) and can often exceed EarthCARE’s goal of being able to, effectively, retrieve properties to within ± 10 W m⁻². The tacit warning here is that continued reliance on just 1D RT models would amount to a heightened rate of radiative closure assessments being unwittingly nullified.

Data availability

635 The EarthCARE Level-2 demonstration products the ACM-COM products discussed in this paper are available from <https://doi.org/10.5281/zenodo.7117115> (van Zadelhoff et al. 2022) as are “operational” ACM-RT output. Specialized ACM-RT calculations presented in this paper, e.g., with increased photon count, and radiative transfer calculations are available from <https://doi.org/10.5281/zenodo.7272662> (Cole et al. 2022).

Competing interests

640 The authors have no competing interests to declare.

Author contributions

HWB drafted the manuscript, developed the ACM-RT and ACM-COM algorithms, and the 3D solar radiative transfer model used in ACM-RT. JNSC developed the ACM-RT processor software and the 3D thermal radiative transfer model, performed all ACM-RT calculations, and drafted sections of the manuscript. ZQ developed ACM-COM’s
645 algorithms and software plus aerosol look-up table for ACM-RT. NV contributed to development and testing of ACM-RT and performed independent 3D solar radiative transfer calculations. MS integrated the 1D RRTMG model

into ACM-RT. All authors were involved in development of ACM-RT and ACM-COM and contributed material and text to the manuscript.

Acknowledgements

650 We are especially indebted to Dr. Tobias Wehr, who passed away on 1-Feb-2023, for his unwavering support and encouragement over many years of work. We also wish to thank Michael Eisinger and all EarthCARE algorithm development team members for their ongoing support.

References

655 Alvarado, M.J., V. H. Payne, E. J. Mlawer, G. Uymin, M. W. Shephard, K. E. Cady-Pereira, J. S. Delamere, and J.-L. Moncet, 2012: Performance of the line-by-line radiative transfer model (LBLRTM) for temperature, water vapor, and trace gas retrievals: Recent updates evaluated with IASI case studies, submitted to ACPD acp-2012-813.

660 Barker, H. W., R. K. Goldstein, and D. E. Stevens, 2003: Monte Carlo simulation of solar reflectances for cloudy atmospheres. *J. Atmos. Sci.*, **60**, 1881-1894.

Barker, H. W., J. N. S. Cole, J. Li, B. Yi, and P. Yang, 2015a: Estimation of Errors for Two-Stream Approximations of the Solar Radiative Transfer Equation for Cloudy Atmospheres. *J. Atmos. Sci.*, **72**, 4053-4074.

665 Barker, H. W., J. N. S. Cole, C. Domenech, M. Shephard, C. Sioris, F. Tornow, and T. Wehr, 2015b: Assessing the Quality of Active-Passive Satellite Retrievals using Broadband Radiances. *Q. J. R. Meteorol. Soc.*, **141**, 1294–1305, DOI:10.1002/qj.2438.

Barker, H. W., M. P. Jerg, T. Wehr, S. Kato, D. Donovan, and R. Hogan, 2011: A 3D Cloud Construction Algorithm for the EarthCARE satellite mission. *Q. J. R. Meteorol. Soc.*, DOI:10.1002/qj.824

Barker, H. W., Z. Qu, S. Belair, S. Leroyer, J. A. Milbrandt, P. A. Vaillancourt, 2017: Scaling Properties of Observed and Simulated Satellite Visible Radiances. *J. Geophys. Res.*, **122**, 9413– 9429, doi:10.1002/2017JD027146.

670 Barker, H. W., J. N. S. Cole, Z. Qu, N. Villefranque, and M. W. Shephard, 2023 : Radiative closure assessment of retrieved cloud and aerosol properties for the EarthCARE mission: the ACMB-DF product. *Atmospheric Measurement Techniques*, to be submitted.

Baum, B. A., P. Yang, A. J. Heymsfield, C. Schmitt, Y. Xie, A. Bansemer, Y. X. Hu, and Z. Zhang, 2011: Improvements to shortwave bulk scattering and absorption models for the remote sensing of ice clouds. *J. Appl. Meteor. Clim.*, **50**, 1037-1056.

675 Case, K. M., 1957: Transfer problems and the reciprocity principle. *Reviews of Modern Physics*, **29**, 651-663.

Chýlek, P., P. Damiano, and E. P. Shettle, 1992: Infrared emittance of water clouds, *J. Atmos. Sci.*, **49**, 1459–1472.

680 Clough, S. A., M. W. Shephard, E. J. Mlawer, J. S. Delamere, M. J. Iacono, K. Cady-Pereira, S. Boukabara, and P. D. Brown, 2005: Atmospheric radiative transfer modeling: a summary of the AER codes, Short Communication, *J. Quant. Spectrosc. Radiat. Transfer*, **91**, 233-244.

Cole, J. N. S. 2005: *Assessing the importance of Unresolved Cloud-Radiation Interactions in Atmospheric Global Climate Models Using the Multiscale Modelling Framework*. PhD thesis, The Pennsylvania State University, University Park.

685 Cole, Jason N. S., H. W. Barker, Z., Qu, N., Villefranque, and M. W. Shephard, 2022 : Enhanced 3D radiative transfer ACM-RT calculations and output for Cole et al., 2022 [Data set]. Zenodo. <https://doi.org/10.5281/zenodo.7272662>

Cotton, W. R. and N. R. Gokhale, 1967: Collision, coalescence and breakup of large water drops in a vertical wind tunnel. *J. Geophys. Res.* **72**, 4041–4049.

690 Cox C. and W. Munk, 1956: Slopes of the sea surface deduced from photographs of the sun glitter. *Bull Scripps Inst Oceanog.* **6**, 401–488.

Diner, D. J. and J. V. Martonchik, 1984: Atmospheric transfer of radiation above an inhomogeneous non-Lambertian ground: 1 – Theory. *J. Quant. Spectrosc. Radiat. Trans.*, **31**, 97–125.

695 Donovan, D., G.-J., van Zadelhoff, and P. Wang 2023: The ATLID L2a profile processor (A-AER, A-EBD, A-TC and A-ICE products). *Atmospheric Measurement Techniques*, to be submitted.

Donovan, D., P. Kollias, and G.-J. van Zadelhoff, 2023: The Generation of EarthCARE L1 Test Data sets Using Atmospheric Model Data Sets. *Atmospheric Measurement Techniques*, to be submitted.

700 Ellingson, R. G. and E. E. Takara, 2005: Longwave Radiative Transfer in Inhomogeneous Cloud Layers. Pg 487 - 519 in *Three-dimensional Cloud Structure and Radiative Transfer*. Eds. A. Marshak and A., Davis. Springer-Verlag, 686pp.

Eisinger, M., T. Wehr, T., Kubota, D., Bernaerts, and K. Wallace, 2023: The EarthCARE production model and auxiliary products. *Atmospheric Measurement Techniques*, to be submitted.

ESA., 2001: *The Five Candidate Earth Explorer Missions: EarthCARE –Earth Clouds, Aerosols and Radiation Explorer*, ESA SP-1257(1), September 2001. ESA Publications Division: Noordwijk, The Netherlands.

705 Fauchez, T., A. Davis, C. Cornet, F. Szczap, S. Platnick, et al., 2017: A fast hybrid (3-D/1-D) model for thermal radiative transfer in cirrus via successive orders of scattering. *J. Geophys. Res.*, **122** (1), 344-366. 10.1002/2016JD025607.

Friedman, D., 1969: Infrared characteristics of ocean water. *Appl. Opt.*, **8**, 2073-2078.

710 Goody, R. M., R. West, L. Chen, and D. Crisp, 1989: The correlated k-distribution method for radiation calculation in nonhomogeneous atmospheres. *J. Quant. Spectrosc. Radiat. Transfer*, **42**, 539–550, doi:10.1016/0022-4073(89)90044-7.

Hale, G. M. and M. R. Querry, 1973: Optical constants of water in the 200nm to 200 μ m wavelength region. *Appl. Opt.*, **12**, 555-563.

715 Hansen, J., G. Russell, D. Rind, P. Stone, A. Lacis, S. Lebedeff, R. Ruedy, and L. Travis, 1983: Efficient three-dimensional global models for climate studies: models i and ii. *Mon. Wea. Rev.*, **111**, 609–662.

Henyey, L. G., and J. L. Greenstein, 1941: Diffuse light in the galaxy. *Astro. Phys. J.*, **93**, 70.

Hogan, R. J., S. A. K. Schäfer, C. Klinger, J.-C. Chiu, and B. Mayer, 2016: Representing 3D cloud-radiation effects in two-stream schemes: 2. Matrix formulation and broadband evaluation. *J. Geophys. Res. Atmos.*, **121**, 8583–8599, <https://doi.org/10.1002/2016JD024875>.

720 Hogan, R. J., M. D. Fielding, H. W. Barker, N. Villefranque, and S. A. K. Schafer, 2019: Entrapment: An important mechanism to explain the shortwave 3D radiative effect of clouds. *J. Atmos. Sci.*, **76**, 2123-2141.

Hu Y. X., and Stammes, 1993: An accurate parameterization of the radiative properties of water clouds suitable for use in climate models. *J. Climate*, **6**, 728-742.

725 Huang, X., Chen, X., Zhou, D. K., & Liu, X.: An observationally based global band-by-band surface emissivity dataset for climate and weather simulations. *J. Atmos. Sci.*, **73**(9), 3541– 3555. <https://doi.org/10.1175/jas-d-15-0355.1>, 2016.

Hünerbein, A., S. Bley, H., Deneke, J. F., Meirink, G.-J., van Zadelhoff, and A. Walther, 2023: Cloud optical and physical property retrievals from the EarthCARE multi-spectral imager: the M-COP product. *Atmospheric Measurement Techniques*, to be submitted.

730 Iacono, M. J., J. S. Delamere, E. J. Mlawer, and S. A. Clough, 2003: Evaluation of upper tropospheric water vapor in the NCAR Community Climate Model, CCM3, using modeled and observed HIRS radiances. *J. Geophys. Res.*, **108**, 4037, doi:10.1029/2002JD002539.

Iacono, M. J., J. S. Delamere, E. J. Mlawer, M. W. Shephard, S. A. Clough, and W. D. Collins, 2008: Radiative forcing by long-lived greenhouse gases: Calculations with the AER radiative transfer models, *J. Geophys. Res.*, **113**, D13103, doi:10.1029/2008JD009944.

735 Illingworth, A. + others, 2015: THE EARTHCARE SATELLITE: The next step forward in global measurements of clouds, aerosols, precipitation and radiation. *Bull. Am. Met. Soc.*, **96**, 1311-1332. DOI:10.1175/BAMS-D-12-00227.1.

Irbah, A., J. Delanoe, G.-J., Zadelhoff, D., Donovan, P., Kollias, A., Tatarevic, B. P., Treserras, S., Mason, S., and Hogan 2023: The classification of atmospheric hydrometeors and aerosols from EarthCare radar and lidar: the A-TC, C-TC and AC-TC products. *Atmospheric Measurement Techniques*, to be submitted.

740 Iwabuchi, H., 2006: Efficient Monte Carlo methods for radiative transfer modeling. *J. Atmos. Sci.*, **63**, 2324-2339.

Kato, S., N. G. Loeb, F. G. Rose, D. R. Doelling, D. A. Rutan, T. E. Caldwell, L. Yu, and R. A. Weller, 2013: Surface irradiances consistent with CERES-derived top-of-atmosphere shortwave and longwave irradiances. *J. Clim.*, **26**, 2719–2740.

745 Lacis, A. A., and V. Oinas, 1991: A description of the correlated k-distribution method for modeling nongray gaseous absorption, thermal emission, and multiple scattering in vertically inhomogeneous atmospheres. *J. Geophys. Res.*, **96**, 9027–9074, doi:10.1029/90JD01945.

750 L'Ecuyer, T., N. Wood, T. Haladay, G. L. Stephens, and P. W. Stackhouse, 2008: Impact of clouds on atmospheric heating based on the R04 CloudSat fluxes and heating rates dataset. *J. Geophys. Res.*, **113**:D00A15. doi:10.1029/2008JD009951.

Li, J. and V. Ramaswamy, 1996: Four-Stream Spherical Harmonic Expansion Approximation for Solar Radiative Transfer. *J. Atmos. Sci.*, **53**, 1174–1186.

755 Loeb, N. G., S. Kato, and B. A. Wielicki, 2002: Defining Top-of-the-Atmosphere Flux Reference Level for Earth Radiation Budget Studies. *J. Climate*, **15**, 3301-3309.

Marchuk, G. I., G. A. Mikhailov, M. A. Nazaraliev, R. A. Darbinjan, B. A. Kargin, and B. S. Elepov, 1980: *Monte Carlo Methods in Atmospheric Optics*. Optical Science Series, 12, Springer Verlag, 208 pp.

Marshall, J. S. and W. M. Palmer, 1948: The distribution of raindrops with size. *J. of Meteor.*, **5** (4), 165–166.

760 Mason, S., R. J. Hogan, A., Bozzo, and N. Pounder, 2023: A unified synergistic retrieval of clouds, aerosols and precipitation from EarthCARE: the ACM-CAP product, 2022: EGUSphere [preprint], <https://doi.org/10.5194/egusphere-2022-1195>. Mason, S., R. J. Hogan, D., Donovan, G.-J., van Zadelhoff, P., Kollias, B. P., Treserras, and Z., Qu, 2023a: An intercomparison of EarthCARE cloud, aerosol and precipitation retrieval products. *Atmospheric Measurement Techniques*, to be submitted.

Masuda, K., T. Takashima, and Y. Takayama, 1988: Emissivity of pure and sea waters for the model sea surface in the infrared window regions. *Rem. Sens. Env.*, **24**, 313-329

765 Milbrandt, J. A., S. Béclair, M. Faucher, M. Vallée, M. L. Carrera, and A. Glazer, 2016: The Pan-Canadian high resolution (2.5km) deterministic prediction system. *Weather and Forecasting*, **31**, 1791-1816.

Mlawer, E. J., S. J. Taubman, P. D. Brown, M. J. Iacono, and S. A. Clough, 1997: Radiative transfer for inhomogeneous atmospheres: RRTM, a validated correlated-k model for the longwave. *J. Geophys. Res.*, **102**, 16 663–16 682, doi:10.1029/97JD00237.

770 Mlawer, E. J., and S. A. Clough, 1998: Shortwave and longwave enhancements in the rapid radiative transfer model. Proc. Seventh Atmospheric Radiation Measurement (ARM) Science Team Meeting, San Antonio, TX, U.S. Dept. of Energy, 409–413. [Available online at https://www.arm.gov/publications/proceedings/conf07/extended_abs/mlawer_ej.pdf.]

775 Modest, M. F., 2003: Backward Monte Carlo simulations in radiative heat transfer. *ASME Journal of Heat Transfer*, **125**, 57-62.

Morcrette, J.-J., H.W. Barker, J.N.S. Cole, M.J. Iacono, and R. Pincus, 2008: Impact of a new radiation package, McRad, in the ECMWF Integrated Forecasting System. *Mon. Wea. Rev.*, **136**, 4773–4798.

780 Mroz, K., B. P. Treserras, A., Battaglia, P. Kollias, A. Tatarevic, and F. Tridon, 2023 : Cloud and Precipitation Microphysical Retrievals from the EarthCARE Cloud Profiling Radar: the C-CLD product, EGUSphere [preprint], <https://doi.org/10.5194/egusphere-2023-56>.

Oreopoulos, L., and Coauthors, 2012: The continual intercomparison of radiation codes: Results from Phase I. *J. Geophys. Res.*, **117**, D06118, doi:10.1029/2011JD016821.

785 Qu, Z., D. P. Donovan, H. W., Barker, J. N. S., Cole, and M. W. Shephard, and V. Huijnen, 2022: Numerical model generation of test frames for pre-launch studies of EarthCARE's retrieval algorithms and data management system. *Atmos. Meas. Tech. Discuss.* [preprint], <https://doi.org/10.5194/amt-2022-300>, in review.

Qu, Z., H. W. Barker, J. N. S. Cole, and M. W. Shephard, 2023: Across-track extension of retrieved cloud and aerosol properties for the EarthCARE mission: the ACMB-3D product, *Atmos. Meas. Tech.*, **16**, 2319–2331, <https://doi.org/10.5194/amt-16-2319-2023>.

790 Rahman, H., Pinty, B. and Verstraete, M.M., 1993, Coupled surface-atmosphere reflectance (CSAR) model 2. Semiempirical surface model usable with NOAA Advanced Very High Resolution Radiometer data. *J. Geophys. Res.*, **98**, 20,791–20,801.

795 Schaaf, C. B., F. Gao, A. H. Strahler, W. Lucht, X. Li, T. Tsang, N. C. Strugnell, X. Zhang, Y. Jin, J.-P. Muller, P. Lewis, M. Barnsley, P. Hobson, M. Disney, G. Roberts, M. Dunderdale, C. Doll, R. d'Entremont, B. Hu, S. Liang, and J. L. Privette, 2002: First Operational BRDF, Albedo and Nadir Reflectance Products from MODIS, *Remote Sens. Environ.*, **83**, 135–148.

Segelstein, D., 1981: "The Complex Refractive Index of Water", M.S. Thesis, University of Missouri--Kansas City.

800 Shephard M. W., S. A. Clough, V. H. Payne, W. L. Smith, S. Kireev, and K. E. Cady-Pereira, 2009: Performance of the line-by-line radiative transfer model (LBLRTM) for temperature and species retrievals: IASI case studies from JAIVEx. *Atmos. Chem. Phys.*, **9**, 7397–7417.

Stephens, G.L., Vane, D.G., Boain, R.J., Mace, G.G., Sassen, K., Wang, Z., Ilingworth, A.J., O'Connor, E.J., Rossow, W.B., Durden, S.L., Miller, S.D., Austin, R.T., Benedetti, A., Mitrescu, C., and the CloudSat Science Team., 2002: The CloudSat mission and the A-Train: A new dimension of space-based observations of clouds and precipitation. *Bull. Amer. Meteor. Soc.*, **83**, 1771–1790, <https://doi.org/10.1175/BAMS-83-12-1771>.

805 Ulbrich, C. W., 1983: Natural variations in the form of raindrop size distribution. *J. Clim. Appl. Met.*, **22**, 1764–1775.

van Zadelhoff, G.-J., H. W., Barker, E., Baudrez, S., Bley, N., Clerbaux, J. N. S., Cole, J., de Kloe, N., Docter, C., Domenech, D. P., Donovan, J.-L. Dufresne, M., Eisinger, J., Fischer, R., García-Marañón, M., Haarig, R. J., Hogan, A., Hünerbein, P., Kollas, R., Koopman, T., Wehr, 2022: EarthCARE level-2 demonstration products from simulated scenes (09.01) [Data set]. Zenodo. <https://doi.org/10.5281/zenodo.7117116>

810 Velázquez-Blázquez, A., E. Baudrez, N., Clerbaux, C., Domenech, R. G., Marañón, and N. Madenach, 2023a: Towards instantaneous top-of-atmosphere fluxes from EarthCARE: The BMA-FLX product. *Atmospheric Measurement Techniques*, to be submitted.

815 Velázquez-Blázquez, A., E. Baudrez, N., Clerbaux, and C. Domenech, 2023b: Unfiltering of the EarthCARE Broadband Radiometer (BBR) observations: the BM-RAD product. *Atmospheric Measurement Techniques*, to be submitted.

Villefranque, N., R. Fournier, F. Couvreux, S. Blanco, C. Cornet, V. Eymet, V. Forest, and J.-M. Tregan, 2019: A Path-Tracing Monte Carlo Library for 3-D Radiative Transfer in Highly Resolved Cloudy Atmospheres, *J. Adv. Model. Earth Syst.*, **11**, 2449–2473. doi:<https://doi.org/10.1029/2018MS001602>.

820 Walters, D. V. and R. O. Buckius, 1992: Rigorous development for radiation heat transfer in nonhomogeneous absorbing, emitting and scattering media. *Int. J. Heat Mass Transfer*, **35**, 3323–3333.

Wandinger, U., A. A. Floutsi, H. Baars, M. Haarig, A. Ansmann, A. Hünerbein, N. Docter, D. Donovan, G.-J. van Zadelhoff, S. Mason, and J. Cole, 2023: HETEAC – the Hybrid End-To-End Aerosol Classification model for EarthCARE, *Atmos. Meas. Tech.*, **16**, 2485–2510, <https://doi.org/10.5194/amt-16-2485-2023>, 2023.

825 Wielicki, B. A., B. R. Barkstrom, E. F. Harrison, R. B. Lee III, G. L. Smith, and J. E. Cooper, 1996: Clouds and the Earth's Radiant Energy System (CERES): An Earth Observing System experiment. *Bull. Amer. Meteor. Soc.*, **77**, 853–868.

Wiscombe, W. J., 1980: Improved Mie scattering algorithms. *Appl. Opt.*, **19**, 1505-1509.

Wiscombe W. J., 1977: The Delta-M Method: Rapid yet accurate radiative flux calculations for strongly asymmetric phase functions *J. Atmos. Sci.*, **34**, 1408-1422.

830 Wu, X. and W.L. Smith, 1997: Emissivity of rough sea surface for 8-13 μ m: modeling and verification. *Appl. Opt.*, **36**, 2609-2619.

Yang, P., L. Bi, B. A. Baum, K.-N. Liou, G. Kattawar, M. Mishchenko, and B. Cole, 2013: Spectrally consistent scattering, absorption, and polarization properties of atmospheric ice crystals at wavelengths from 0.2 μ m to 100 μ m. *J. Atmos. Sci.*, **70**, 330-347.

835